Line-of-Sight MIMO via Intelligent Reflecting Surface

Heedong Do, *Graduate Student Member, IEEE*, Namyoon Lee, *Senior Member, IEEE*, Angel Lozano, *Fellow, IEEE*

***Abstract*—This paper deals with line-of-sight (LOS) MIMO communication via an intelligent reflecting surface (IRS). It is shown that the number of spatial degrees of freedom (DOF) afforded by this setting grows in proportion with the IRS aperture, as opposed to being dictated by the transmit and receive apertures; this buttresses the interest in IRS deployments at mmWave and terahertz frequencies, with wavelengths and transmission ranges small enough to enable LOS MIMO. Explicit and simple-to-implement IRS phase shifts are put forth that achieve, not only the maximum number of DOF, but the capacity, under a certain geometrical condition. The insights leading to the proposed phase shifts, and to the optimality condition itself, are asymptotic in nature, yet extensive simulations confirm that the performance is excellent for a broad range of settings and even if the optimality condition is not strictly met.**

***Index Terms*—Line-of-sight transmission, MIMO, multi-antenna channels, mmWave frequencies, terahertz frequencies, intelligent reflecting surface**

I. Introduction

The terahertz (THz) frequency band, broadly defined as 0.1–10 THz, is arguably the next frontier in the evolution of wireless systems [1]–[3], with a comprehensive set of experiments at frequencies above 100 GHz being summarized in [4, Fig. 1]. This band is challenging in terms of radio propagation and its envisioned applications are predominantly of a short-range nature. Owing to the lack of diffraction, communication is highly contingent on either a line-of-sight (LOS) component or strong reflections. At the same time, the conjunction of a tiny wavelength and such short transmission range opens the door to multiple-input multiple-output (MIMO) transmission with arrays of very reasonable physical dimensions in LOS [5]–[14]. Indeed, as the radio wavefront curvature becomes noticeable over the transmit and receive arrays, the channel matrix acquires plural rank even in sheer LOS [15]–[21]. Altogether then, LOS conditions are ideal for THz communication as they ensure the best possible pathloss and the possibility of spatial multiplexing.

LOS MIMO exhibits a behavior that contrasts starkly with the familiar one in rich multipath MIMO, where the number of spatial degrees of freedom (DOF) is known to scale with the smallest of transmitter and receiver [22]. This different behavior can be traced back to the nature of the channel itself. While, in a multipath channel, the environment acts as a large aperture—in essence a lens—through which the receiver can resolve each individual transmit antenna and vice versa, in LOS MIMO the transmit and receiver apertures themselves provide that resolution. Thus, enlarging the receiver enables packing antennas more closely at the transmitter and vice versa, as a larger aperture at either end of the link enables a finer resolution of the other end. The result is that the DOF scales with the *product* of the transmit and receive apertures, or more precisely the projections of these apertures on a plane orthogonal to the link. Referring to Fig. 1, the DOF in LOS MIMO satisfy [23], [24] (see also [25], [26])

$$\mathsf{DOF} \approx \frac{A_{\mathrm{t}} A_{\mathrm{r}}}{(\lambda D)^2} \tag{1}$$

where λ is the wavelength and the approximation sharpens as the arrays grow large.

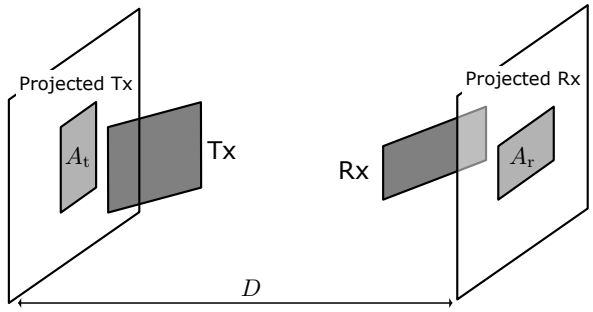

Fig. 1. LOS MIMO setting with a range D and with A_{t} and A_{r} the projections of the transmit and receive apertures on a plane orthogonal to the link.

Of late, intelligent reflecting surfaces (IRSs) are emerging as a form of non-regenerative relays that are passive, devoid of radio-frequency chains and baseband processing; each composing element merely reradiates the impinging wave with a certain phase shift [27]–[35]. In the THz band it is important, as advanced, to explicitly model the curved nature of the wavefronts; several recent works explore this paradigm for IRS-assisted communication [36]–[38]. For single-input single-output (SISO), beamforming based on far-field steering vectors at the IRS, ignoring the wavefront curvature, is shown to be highly suboptimum [36]. Then, [37] considers LOS propagation with multiple IRSs whose phase shifts are

H. Do is with POSTECH, 37673 Pohang (e-mail: doheedong@postech.ac.kr) and N. Lee is with Korea University, 02841 Seoul (e-mail: namyoon@korea.ac.kr). Their work is supported by Institute of Information & communications Technology Planning & Evaluation (IITP) (No.2021-0-00161, Post MIMO system research for massive connectivity and new wireless spectrum) and by the National Research Foundation of Korea (NRF) grant (No. 2020R1C1C1013381) funded by the Korea government (MSIP). A. Lozano is with Univ. Pompeu Fabra, 08018 Barcelona (e-mail: angel.lozano@upf.edu). His work is supported by the European Research Council under the H2020 Framework Programme/ERC grant agreement 694974, by ICREA, and by MSCA-ITN-ETN 956256 “Meta Wireless”.

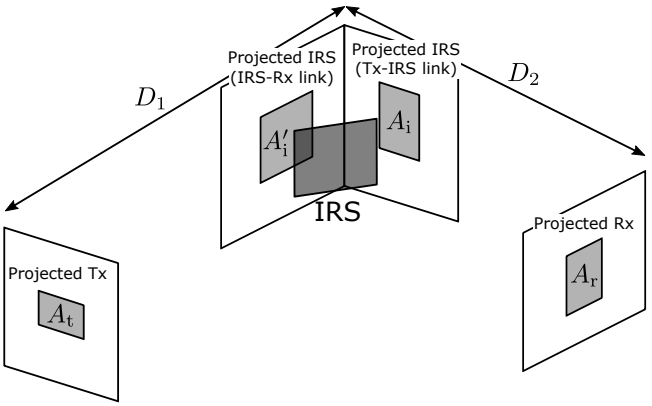

Fig. 2. Cascaded LOS MIMO links with an IRS that serves as receiver for the first link and transmitter for the second link. Both IRS projections scale with the IRS size, hence enlarging the IRS simultaneously enriches the DOF of both links.

optimized to maximize the spectral efficiency. However, the arrays are too small for meaningful spatial multiplexing: the second singular value of the transmitter-IRS channel is 26 dB below the main one. This implies that, because of the exceedingly small apertures, the spherical wavefront under consideration is, in effect, hardly different from a planar model. In [38], assuming that both transmitter and receiver feature uniform linear arrays (ULAs), the distance pairs where both the transmitter-IRS and the IRS-receiver channels can be orthogonal when appropriately oriented are partly characterized.

This work considers IRS-assisted MIMO transmission at THz frequencies, with LOS from transmitter to IRS and from IRS to receiver, and without the benefit (due to blockage) of a direct path. Transmitter, receiver, and IRS feature arrays that are uniform and planar (UPAs), but otherwise arbitrary. The thrust of the paper is the idea that, because the DOF in LOS MIMO increase with the product of the transmit and receive apertures, the cascading of two LOS MIMO links via an IRS—that serves as receiver for the first link and transmitter for the second link—could exhibit a number of DOF that scales with the size of such IRS, even if the end transmitter and receiver are fixed in size (see Fig. 2). The presented analysis confirms that this is the case. Namely, under an easy-to-meet condition expounded in the paper,

$$\mathsf{DOF} \approx \min\left(\frac{A_{\rm t}A_{\rm i}}{(\lambda D_1)^2}, \frac{A_{\rm r}A'_{\rm i}}{(\lambda D_2)^2}\right), \tag{2}$$

which again sharpens with the aperture sizes and which contrasts sharply with what unfolds with environmental reflections or conventional reflecting devices [39]; at best, those yield a prolonged LOS path and hence a preservation of the number of DOF dictated by transmitter and receiver.

A subsidiary question that arises is how to configure the IRS such that the DOF indeed scale with its size as per (2). Inspired by the observation that, in various limiting regimes, the DOF are maximized when the IRS phase shifts correct for the curvatures of both the impinging and departing wavefronts, we propose this solution in full generality and assess its performance in a broad range of settings. In conjunction with the optimum MIMO precoder and receiver, these phase shifts do perform almost optimally, not only in terms of DOF but of capacity, regardless of the range, relative positions, and orientations.

Altogether, the distinguishing attributes of the paper are:

- The use of an IRS, not to beamform, but to act as a lens that augments the number of DOF available for LOS spatial multiplexing. A larger IRS enables packing antennas more tightly at both transmitter and receiver.
- The derivation of an explicit and easy-to-implement solution for the IRS phase shifts that enable the above behavior.
- The inclusion of physically-motivated amplitude variations in the IRS model, rather than only pure phase shifts.

The manuscript is organized as follows. Section II introduces the point-to-point LOS channel model and its small-aperture approximation while Section III extends the setup to incorporate an IRS. It is shown that, when the IRS is set to reflect, the number of DOF is limited by the transmit and receive apertures. Also, a capacity upper bound is derived as benchmark. Thereafter, IRS phase shifts that compensate for the cascaded curvatures of the wavefronts are proposed to transcend the DOF limits imposed by the transmit and receive apertures. The channel model is specialized to planar arrays in Section IV. Then, Section V introduces a representation that is accurate for dense arrays. Armed with this toolkit, Section VI analyzes the DOF of the proposed solution and shows that such solution is DOF-optimal under an intuitive condition. This proposed solution is numerically evaluated against the capacity upper bound in Section VII, confirming its effectiveness in a broad range of situations. Finally, the paper concludes in Section VIII.

II. LOS Channel Model

As the key building block, consider an LOS MIMO channel with $N_{\rm t}$ transmit and $N_{\rm r}$ receive antennas. Denoting by $D_{n,m}$ the distance from the mth transmit to the nth receive antenna, the complex baseband channel coefficient is given by

$$h_{n,m} = \frac{\sqrt{G_{\rm t}G_{\rm r}}\,\lambda}{4\pi\, D_{n,m}}\, e^{-j\frac{2\pi}{\lambda}D_{n,m}} \qquad \begin{matrix} n=1,\ldots,N_{\rm r} \\ m=1,\ldots,N_{\rm t} \end{matrix} \tag{3}$$

where $G_{\rm t}$ and $G_{\rm r}$ are the transmit and receive antenna gains, respectively. Under the proviso that both arrays are sufficiently small relative to every $D_{n,m}$, it holds that $D_{n,m} \approx D$ $\forall m,n$. It should be stressed, though, that this does not imply $e^{-j\frac{2\pi}{\lambda}D_{n,m}} \approx e^{-j\frac{2\pi}{\lambda}D}$. Factoring out $|h_{n,m}|$, the channel matrix satisfies

$$\boldsymbol{H} \approx \begin{bmatrix} e^{-j\frac{2\pi}{\lambda}D_{1,1}} & \ldots & e^{-j\frac{2\pi}{\lambda}D_{1,N_{\rm t}}} \\ \vdots & \ddots & \vdots \\ e^{-j\frac{2\pi}{\lambda}D_{N_{\rm r},1}} & \ldots & e^{-j\frac{2\pi}{\lambda}D_{N_{\rm r},N_{\rm t}}} \end{bmatrix}. \tag{4}$$

Cartesian coordinates are adopted, with transmitter and receiver in the vicinity of $(0,0,0)$ and $(0,0,D)$, and with (x_m, y_m, z_m) and (x'_n, y'_n, z'_n) the locations of the mth

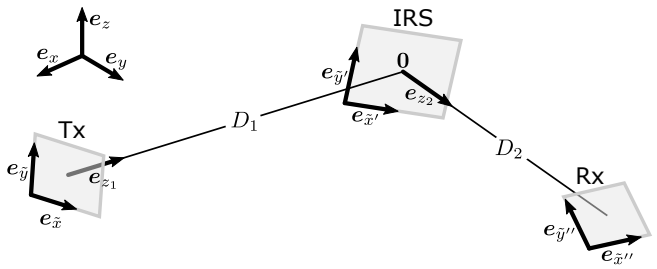

Fig. 3. Coordinate systems: $\{\boldsymbol{e}_{\tilde{x}}, \boldsymbol{e}_{\tilde{y}}\}$, $\{\boldsymbol{e}_{\tilde{x}'}, \boldsymbol{e}_{\tilde{y}'}\}$, and $\{\boldsymbol{e}_{\tilde{x}''}, \boldsymbol{e}_{\tilde{y}''}\}$ are principal axes of the transmit array, IRS, and receive array, respectively, as described in Sec. IV-C.

transmit and nth receive antenna, respectively. The small-aperture approximation then boils down to $\|(x_m, y_m, z_m)\|$ and $\|(x'_n, y'_n, z'_n) - (0, 0, D)\|$ being small relative to D, such that

$$D_{n,m} = \sqrt{(x'_n - x_m)^2 + (y'_n - y_m)^2 + (z'_n - z_m)^2} \tag{5}$$

$$= (z'_n - z_m) \cdot \sqrt{1 + \frac{(x'_n - x_m)^2 + (y'_n - y_m)^2}{(z'_n - z_m)^2}} \tag{6}$$

$$\approx (z'_n - z_m) \left(1 + \frac{(x'_n - x_m)^2 + (y'_n - y_m)^2}{2(z'_n - z_m)^2}\right) \tag{7}$$

$$\approx (z'_n - z_m) + \frac{(x'_n - x_m)^2 + (y'_n - y_m)^2}{2D} \tag{8}$$

with (7) corresponding to the Fresnel or paraxial approximation in optics [40]–[42] for $z_m = 0$ and $z'_n = D$. The validity of this approximation is examined in [40, Ch. 4.2.2] and references therein. In the sequel, the analysis rests on the obtained channel model

$$[\boldsymbol{H}]_{n,m} = e^{-j\frac{2\pi}{\lambda}\left((z'_n - z_m) + \frac{(x'_n - x_m)^2 + (y'_n - y_m)^2}{2D}\right)}, \tag{9}$$

yet all the numerical results in Sec. VII rely on the exact model in (3).

Expanding the squares in (9),

$$[\boldsymbol{H}]_{n,m} = e^{-j\frac{2\pi}{\lambda}\left(z'_n + \frac{(x'_n)^2 + (y'_n)^2}{2D}\right)} \cdot e^{j\frac{2\pi}{\lambda D}((x'_n, y'_n)\cdot(x_m, y_m))} \cdot e^{-j\frac{2\pi}{\lambda}\left(-z_m + \frac{x_m^2 + y_m^2}{2D}\right)}, \tag{10}$$

where the leading and trailing (nonlinear) terms can be compensated with per-antenna phase shifts at receiver and transmitter, respectively. The remaining term amounts to a distinct plane wave from each transmit to each receive antenna, in stark contrast with the single plane wave that would be observed in a planar-wavefront paradigm. Moreover, only the projection of the antenna positions onto the xy-plane matters to this central term in (10).

III. LOS MIMO via IRS

A. IRS Channel Model

Consider an N_t-antenna UPA transmitter, an N_r-antenna UPA receiver, and an M-element UPA IRS, with the direct link between transmitter and receiver being blocked. The relation between the transmit signal $\boldsymbol{s}$ and the receive signal $\boldsymbol{y}$ is

$$\boldsymbol{y} = \boldsymbol{H}_2 \boldsymbol{\Phi} \boldsymbol{H}_1 \boldsymbol{s} + \boldsymbol{v} \tag{11}$$

given $\boldsymbol{H}_2 \in \mathbb{C}^{N_\mathrm{r} \times M}$ as the IRS-receiver channel, $\boldsymbol{\Phi} = \mathrm{diag}(e^{j\phi_1}, \ldots, e^{j\phi_M}) \in \mathbb{C}^{M \times M}$ as the phase shift matrix at the IRS, $\boldsymbol{H}_1 \in \mathbb{C}^{M \times N_\mathrm{t}}$ as the transmitter-IRS channel, and $\boldsymbol{v}$ as the white Gaussian noise at the receiver. The composite channel is denoted by $\boldsymbol{H}_{\mathsf{eff}} = \boldsymbol{H}_2 \boldsymbol{\Phi} \boldsymbol{H}_1$.

The coordinate system origin is placed at the center of the IRS and unit vectors $\boldsymbol{e}_{z_1}$ and $\boldsymbol{e}_{z_2}$ are defined so that transmitter and receiver are in the vicinity of $-D_1 \boldsymbol{e}_{z_1}$ and $D_2 \boldsymbol{e}_{z_2}$. We denote the locations of the mth transmit antenna, ℓth IRS element, and nth receive antenna by (x_m, y_m, z_m), $(x'_\ell, y'_\ell, z'_\ell)$, and (x''_n, y''_n, z''_n), respectively. The unit vectors $\boldsymbol{e}_{z_1}$ and $\boldsymbol{e}_{z_2}$ enable two local coordinate systems: one for the transmitter-IRS link and the other for the IRS-receiver link (see Fig. 3). By completing them with $\boldsymbol{e}_{x_1}, \boldsymbol{e}_{y_1}, \boldsymbol{e}_{x_2}, \boldsymbol{e}_{y_2}$ such that both $\{\boldsymbol{e}_{x_1}, \boldsymbol{e}_{y_1}, \boldsymbol{e}_{z_1}\}$ and $\{\boldsymbol{e}_{x_2}, \boldsymbol{e}_{y_2}, \boldsymbol{e}_{z_2}\}$ are orthonormal sets satisfying

$$\boldsymbol{e}_{x_1}\boldsymbol{e}_{x_1}^\top + \boldsymbol{e}_{y_1}\boldsymbol{e}_{y_1}^\top + \boldsymbol{e}_{z_1}\boldsymbol{e}_{z_1}^\top = \boldsymbol{e}_{x_2}\boldsymbol{e}_{x_2}^\top + \boldsymbol{e}_{y_2}\boldsymbol{e}_{y_2}^\top + \boldsymbol{e}_{z_2}\boldsymbol{e}_{z_2}^\top = \boldsymbol{I},$$

following (10), the two channels become (12) and (13), respectively.

The distance-related factors that were normalized out of $\boldsymbol{H}_1$ and $\boldsymbol{H}_2$ are incorporated into

$$\mathsf{SNR} = \mathsf{PL}_1\, \mathsf{PL}_2\, \frac{P}{BN_0} \tag{14}$$

where $\mathsf{PL}_1 = \frac{\lambda^2 G_\mathrm{t} G_\mathrm{i}}{(4\pi D_1)^2}$ and $\mathsf{PL}_2 = \frac{\lambda^2 G_\mathrm{i} G_\mathrm{r}}{(4\pi D_2)^2}$ with P the transmit power, B the bandwidth, and N_0 the noise spectral density. In turn, G_i is the antenna gain at the IRS while D_1 is the transmitter-IRS range and D_2 is the IRS-receiver range. Letting $\boldsymbol{s} \sim \mathcal{N}_\mathbb{C}(\boldsymbol{0}, \boldsymbol{Q})$ and $\boldsymbol{v} \sim \mathcal{N}_\mathbb{C}(\boldsymbol{0}, \boldsymbol{I})$, the power constraint can be written as $\mathrm{tr}(\boldsymbol{Q}) = \mathsf{SNR}$.

B. Spectral Efficiency

Given $\boldsymbol{\Phi}$, the system boils down to point-to-point MIMO. Letting $\boldsymbol{H}_{\mathsf{eff}} = \boldsymbol{U}_{\mathsf{eff}} \boldsymbol{\Sigma}_{\mathsf{eff}} \boldsymbol{V}_{\mathsf{eff}}^*$ be a singular value decomposition, the spectral efficiency achievable with a certain $\boldsymbol{\Phi}$ equals

$$C(\boldsymbol{\Phi}) = \max_{\sum_n p_n = \mathsf{SNR}} \sum_n \log_2\left(1 + p_n\, \sigma_n^2(\boldsymbol{H}_2 \boldsymbol{\Phi} \boldsymbol{H}_1)\right), \tag{15}$$

which corresponds to a transmit signal covariance given by $\boldsymbol{Q} = \boldsymbol{V}_{\mathsf{eff}} \boldsymbol{\Lambda}_Q \boldsymbol{V}_{\mathsf{eff}}^*$ with $\boldsymbol{\Lambda}_Q = \mathrm{diag}(p_1, \ldots, p_{N_\mathrm{t}})$ obtained via waterfilling [43], [44]. The capacity follows from maximizing (15) over $\boldsymbol{\Phi}$.

To benchmark (15) for any specific $\boldsymbol{\Phi}$, it is useful to establish an upper bound thereon. A useful such bound can be obtained by relaxing the unit modulus constraint on the phase shifts, i.e., by replacing $\boldsymbol{\Phi} = \mathrm{diag}(e^{j\phi_1}, \ldots, e^{j\phi_M})$ with a unitary $\boldsymbol{\Phi}$. Letting $\boldsymbol{H}_1 = \boldsymbol{U}_1 \boldsymbol{\Sigma}_1 \boldsymbol{V}_1^*$ and $\boldsymbol{H}_2 = \boldsymbol{U}_2 \boldsymbol{\Sigma}_2 \boldsymbol{V}_2^*$ be singular value decompositions, it is proven in App. A that the optimum unitary matrix is $\boldsymbol{\Phi} = \boldsymbol{V}_2 \boldsymbol{U}_1^*$. Then, $\boldsymbol{y} = \boldsymbol{U}_2 \boldsymbol{\Sigma}_2 \boldsymbol{\Sigma}_1 \boldsymbol{V}_1^* \boldsymbol{s} + \boldsymbol{v}$ and the upper bound boils down to

$$C^{\mathsf{up}} = \max_{\sum_n p_n = \mathsf{SNR}} \sum_n \log_2\left(1 + p_n\, \sigma_n^2(\boldsymbol{H}_1)\, \sigma_n^2(\boldsymbol{H}_2)\right). \tag{16}$$

Interestingly, $\boldsymbol{\Phi} = \boldsymbol{V}_2 \boldsymbol{U}_1^*$ resembles the optimal relay matrix for non-regenerative relays [45].

From the observation that both (15) and (16) can be regarded as point-to-point MIMO capacities, for channels with

$$[\boldsymbol{H}_1]_{\ell,m} = \exp\left(-j\frac{2\pi}{\lambda}\left(\boldsymbol{e}_{z_1}^\top\begin{bmatrix}x'_\ell\\y'_\ell\\z'_\ell\end{bmatrix}+\frac{1}{2D_1}\left(\left\|\begin{bmatrix}x'_\ell\\y'_\ell\\z'_\ell\end{bmatrix}\right\|^2-\left(\boldsymbol{e}_{z_1}^\top\begin{bmatrix}x'_\ell\\y'_\ell\\z'_\ell\end{bmatrix}\right)^2\right)\right)\right)\cdot\exp\left(j\frac{2\pi}{\lambda D_1}\left(\begin{bmatrix}x'_\ell & y'_\ell & z'_\ell\end{bmatrix}(\boldsymbol{I}-\boldsymbol{e}_{z_1}\boldsymbol{e}_{z_1}^\top)\begin{bmatrix}x_m\\y_m\\z_m\end{bmatrix}\right)\right)$$
$$\cdot\exp\left(-j\frac{2\pi}{\lambda}\left(-\boldsymbol{e}_{z_1}^\top\begin{bmatrix}x_m\\y_m\\z_m\end{bmatrix}+\frac{1}{2D_1}\left(\left\|\begin{bmatrix}x_m\\y_m\\z_m\end{bmatrix}\right\|^2-\left(\boldsymbol{e}_{z_1}^\top\begin{bmatrix}x_m\\y_m\\z_m\end{bmatrix}\right)^2\right)\right)\right) \quad (12)$$

$$[\boldsymbol{H}_2]_{n,\ell} = \exp\left(-j\frac{2\pi}{\lambda}\left(\boldsymbol{e}_{z_2}^\top\begin{bmatrix}x''_n\\y''_n\\z''_n\end{bmatrix}+\frac{1}{2D_2}\left(\left\|\begin{bmatrix}x''_n\\y''_n\\z''_n\end{bmatrix}\right\|^2-\left(\boldsymbol{e}_{z_2}^\top\begin{bmatrix}x''_n\\y''_n\\z''_n\end{bmatrix}\right)^2\right)\right)\right)\cdot\exp\left(j\frac{2\pi}{\lambda D_2}\left(\begin{bmatrix}x''_n & y''_n & z''_n\end{bmatrix}(\boldsymbol{I}-\boldsymbol{e}_{z_2}\boldsymbol{e}_{z_2}^\top)\begin{bmatrix}x'_\ell\\y'_\ell\\z'_\ell\end{bmatrix}\right)\right)$$
$$\cdot\exp\left(-j\frac{2\pi}{\lambda}\left(-\boldsymbol{e}_{z_2}^\top\begin{bmatrix}x'_\ell\\y'_\ell\\z'_\ell\end{bmatrix}+\frac{1}{2D_2}\left(\left\|\begin{bmatrix}x'_\ell\\y'_\ell\\z'_\ell\end{bmatrix}\right\|^2-\left(\boldsymbol{e}_{z_2}^\top\begin{bmatrix}x'_\ell\\y'_\ell\\z'_\ell\end{bmatrix}\right)^2\right)\right)\right) \quad (13)$$

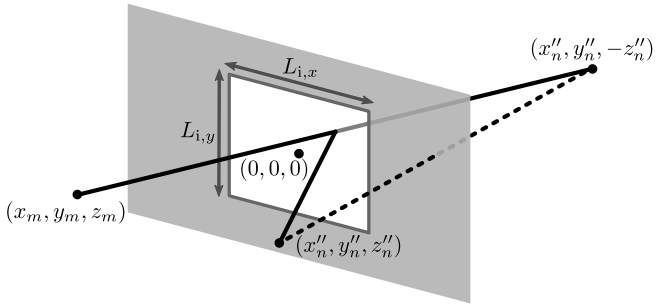

Fig. 4. IRS reflecting a ray-like signal.

singular values $\boldsymbol{\sigma}(\boldsymbol{H}_2\boldsymbol{\Phi}\boldsymbol{H}_1)$ and $\boldsymbol{\sigma}(\boldsymbol{H}_2)\circ\boldsymbol{\sigma}(\boldsymbol{H}_1)$, respectively, it is useful to compare these tuples, where $\circ$ indicates the Hadamard product. If they are sufficiently similar, both bounds are sure to also be similar.

No known procedure exists to identify the optimum phase shifts for a generic channel. Algorithms applying alternating optimization [31] and projected gradient descent [34] have been proposed to find acceptable solutions, albeit with no guarantee of global optimality and with serious real-time implementation issues. In search of explicit solutions, and driven by the interest in spatial multiplexing, we consider the alternative route of maximizing the number of DOF.

C. Simple Reflection

Arguably the simplest use of an IRS would be as a mirror, say with the all-zeros phase shift embodied by $\boldsymbol{\Phi}=\boldsymbol{I}$. Despite the conceptual simplicity of this setting, its analysis is rather involved. In [46], [47], it is considered for a single-antenna setup (under planar wavefronts in [46], and on a two-dimensional environment in [47]). For multiantenna setups, insights can be gleaned by analyzing the composite channel for $\boldsymbol{\Phi}=\boldsymbol{I}$ when $\lambda\to 0$, as a proxy for the tiny wavelengths at THz frequencies. The waves are then ray-like, and the signal reaches the receiver only if the straight line connecting the transmit array with a mirror image of the receive array intersects the IRS (see Fig. 4).

Let the IRS be on the xy-plane, occupying $\left[-\frac{L_{\mathrm{i},x}}{2},\frac{L_{\mathrm{i},x}}{2}\right]\times\left[-\frac{L_{\mathrm{i},y}}{2},\frac{L_{\mathrm{i},y}}{2}\right]$. With no approximations, using (3), the composite channel becomes (17). Without loss of generality, let us assume $z_m, z''_n>0$. As shown in App. B, given that IRS is sufficiently dense, this composite channel is asymptotically identical to (18), where $\mathbf{1}_A(\cdot)$ denotes the indicator function of set A. In (18), the indicator function makes the IRS act as a window. When the IRS is large enough for the indicator function to be immaterial, (18) is identical to the LOS channel between the transmitter and the mirror image (relative to the xy-plane) of the receiver. Therefore, the number of DOF is, at best, what could be achieved without the IRS, and simulations confirm that this limiting result applies for wavelengths and array sizes of interest.

D. Proposed Phase Shifts

Intuition on how to transcend the DOF limits imposed by the transmit and receive apertures can be gathered by taking the array and IRS antenna densities to the limit, a task that we embark on starting in Sec. V. What emerges from that analysis is that the DOF can be enlarged in relation to the size of the IRS if the phase shifts precisely compensate for the cascaded curvatures of the wavefronts that impinge on the IRS and are re-radiated by it, i.e.,

$$\phi_\ell = \frac{2\pi}{\lambda}\left(\boldsymbol{e}_{z_1}^\top\begin{bmatrix}x'_\ell\\y'_\ell\\z'_\ell\end{bmatrix}+\frac{1}{2D_1}\left(\left\|\begin{bmatrix}x'_\ell\\y'_\ell\\z'_\ell\end{bmatrix}\right\|^2-\left(\boldsymbol{e}_{z_1}^\top\begin{bmatrix}x'_\ell\\y'_\ell\\z'_\ell\end{bmatrix}\right)^2\right)\right)$$
$$+\frac{2\pi}{\lambda}\left(-\boldsymbol{e}_{z_2}^\top\begin{bmatrix}x'_\ell\\y'_\ell\\z'_\ell\end{bmatrix}+\frac{1}{2D_2}\left(\left\|\begin{bmatrix}x'_\ell\\y'_\ell\\z'_\ell\end{bmatrix}\right\|^2-\left(\boldsymbol{e}_{z_2}^\top\begin{bmatrix}x'_\ell\\y'_\ell\\z'_\ell\end{bmatrix}\right)^2\right)\right), \quad (19)$$

which, undoing the small-aperture approximation in (5)–(8), can be more succinctly rewritten as

$$\phi_\ell = \frac{2\pi}{\lambda}\cdot\left(\left\|\begin{bmatrix}x'_\ell\\y'_\ell\\z'_\ell\end{bmatrix}+D_1\boldsymbol{e}_{z_1}\right\|^{\frac{1}{2}}-D_1+\left\|D_2\boldsymbol{e}_{z_2}-\begin{bmatrix}x'_\ell\\y'_\ell\\z'_\ell\end{bmatrix}\right\|^{\frac{1}{2}}-D_2\right). \quad (20)$$

$$[\boldsymbol{H}_{\mathsf{eff}}]_{n,m} = \sum_{\ell} \frac{D_1}{\sqrt{(x_n''-x_\ell')^2+(y_n''-y_\ell')^2+(z_n'')^2}} \cdot \frac{D_2}{\sqrt{(x_\ell'-x_m)^2+(y_\ell'-y_m)^2+z_m^2}} \cdot e^{-j\frac{2\pi}{\lambda}\left(\sqrt{(x_n''-x_\ell')^2+(y_n''-y_\ell')^2+(z_n'')^2}+\sqrt{(x_\ell'-x_m)^2+(y_\ell'-y_m)^2+z_m^2}\right)} \tag{17}$$

$$[\boldsymbol{H}_{\mathsf{eff}}]_{n,m} \approx -\frac{j\lambda}{z''+z} \cdot \frac{D_1 D_2}{d_{\mathrm{i},x} d_{\mathrm{i},y}} \cdot \mathbf{1}_{\left[-\frac{L_{\mathrm{i},x}}{2},\frac{L_{\mathrm{i},x}}{2}\right]\times\left[-\frac{L_{\mathrm{i},y}}{2},\frac{L_{\mathrm{i},y}}{2}\right]}(x_0',y_0') \cdot e^{-j\frac{2\pi}{\lambda}\sqrt{(x_n''-x_m)^2+(y_n''-y_m)^2+(z_n''+z_m)^2}}$$
$$\propto \mathbf{1}_{\left[-\frac{L_{\mathrm{i},x}}{2},\frac{L_{\mathrm{i},x}}{2}\right]\times\left[-\frac{L_{\mathrm{i},y}}{2},\frac{L_{\mathrm{i},y}}{2}\right]}(x_0',y_0') \cdot e^{-j\frac{2\pi}{\lambda}\sqrt{(x_n''-x_m)^2+(y_n''-y_m)^2+(z_n''+z_m)^2}} \tag{18}$$

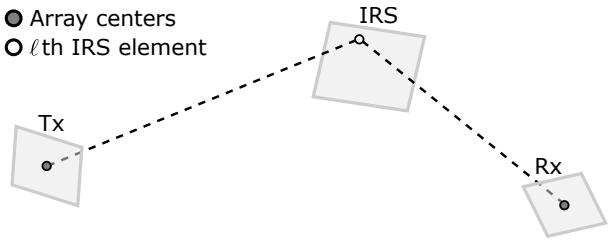

Fig. 5. Intuitive geometric interpretation of the proposed phase shifts in (20).

As the constant terms applied to all IRS elements are immaterial, the above is tantamount to (see Fig. 5)

$$\phi_\ell = 2\pi \frac{\text{length of dotted line}}{\lambda} \tag{21}$$

where the dotted line connects the center of the transmit array with the ℓth IRS element, and then on to the center of the receive array. These phase shifts can be seen as a generalization of beamfocusing [36] and reflective focusing [38]. With these shifts, and with further per-antenna phase shifts at transmitter and receiver that correct for the appropriate terms in (10), the composite channel becomes $\boldsymbol{H}_{\mathsf{eff}} = \boldsymbol{H}_2\boldsymbol{H}_1$ with

$$[\boldsymbol{H}_1]_{\ell,m} = \exp\left(j\frac{2\pi}{\lambda D_1}\left(\begin{bmatrix}x_\ell' & y_\ell' & z_\ell'\end{bmatrix}\left(\boldsymbol{I}-\boldsymbol{e}_{z_1}\boldsymbol{e}_{z_1}^\top\right)\begin{bmatrix}x_m\\y_m\\z_m\end{bmatrix}\right)\right) \tag{22}$$

$$[\boldsymbol{H}_2]_{n,\ell} = \exp\left(j\frac{2\pi}{\lambda D_2}\left(\begin{bmatrix}x_n'' & y_n'' & z_n''\end{bmatrix}\left(\boldsymbol{I}-\boldsymbol{e}_{z_2}\boldsymbol{e}_{z_2}^\top\right)\begin{bmatrix}x_\ell'\\y_\ell'\\z_\ell'\end{bmatrix}\right)\right). \tag{23}$$

The remainder of the paper is devoted to analyzing the performance of (19) for dense arrays and to validating that performance in relation to the capacity upper bound in a broad range of situations. Complementing this, App. C shows that (19) is also optimum in the limit of small transmit and receive apertures, altogether motivating its broad applicability.

Note that (19), which as mentioned compensates for the cascaded curvatures of the impinging and departing wavefronts, can be interpreted as turning the IRS into a lens, rather than a mirror. This lensing role is essentially the same one that the scattering environment plays in multipath-based MIMO, an intuition that further supports the optimality of (19).

IV. Equivalent Channel Model for Planar Arrays

Before proceeding, it is convenient to slightly reformulate the channel matrices and to set forth some properties they satisfy when the arrays are planar.

A. Point-to-Point Channel

Given planar arrays at transmitter and receiver, respectively having their centers at the origin and $D\boldsymbol{e}_z$, we can find orthonormal sets $\{\boldsymbol{e}_{\tilde{x}}, \boldsymbol{e}_{\tilde{y}}\}$ and $\{\boldsymbol{e}'_{\tilde{x}}, \boldsymbol{e}'_{\tilde{y}}\}$ satisfying, for every m and n,

$$\begin{bmatrix}x_m\\y_m\\z_m\end{bmatrix} \in \mathsf{span}\{\boldsymbol{e}_{\tilde{x}}, \boldsymbol{e}_{\tilde{y}}\} \qquad \begin{bmatrix}x_n'\\y_n'\\z_n'\end{bmatrix} \in D\boldsymbol{e}_z + \mathsf{span}\{\boldsymbol{e}_{\tilde{x}'}, \boldsymbol{e}_{\tilde{y}'}\}. \tag{24}$$

Thus, two-dimensional coordinates on the planes, $\begin{bmatrix}\tilde{x}_m & \tilde{y}_m\end{bmatrix}^\top$ and $\begin{bmatrix}\tilde{x}'_n & \tilde{y}'_n\end{bmatrix}^\top$ do exist such that

$$\begin{bmatrix}x_m\\y_m\\z_m\end{bmatrix} = \begin{bmatrix}\boldsymbol{e}_{\tilde{x}} & \boldsymbol{e}_{\tilde{y}}\end{bmatrix}\begin{bmatrix}\tilde{x}_m\\\tilde{y}_m\end{bmatrix} \qquad \begin{bmatrix}x_n'\\y_n'\\z_n'\end{bmatrix} = D\boldsymbol{e}_z + \begin{bmatrix}\boldsymbol{e}_{\tilde{x}'} & \boldsymbol{e}_{\tilde{y}'}\end{bmatrix}\begin{bmatrix}\tilde{x}'_n\\\tilde{y}'_n\end{bmatrix}. \tag{25}$$

Plugging the above into the central term in (10), and recalling once more that the leading and trailing terms in (10) can be compensated with per-antenna phase shifts, we obtain

$$[\boldsymbol{H}]_{n,m} = e^{j2\pi(\boldsymbol{r}_n\cdot\boldsymbol{t}_m)} \tag{26}$$

where

$$\boldsymbol{t}_m = \frac{1}{\sqrt{\lambda D}}\begin{bmatrix}\boldsymbol{e}_x^\top\\\boldsymbol{e}_y^\top\end{bmatrix}\begin{bmatrix}\boldsymbol{e}_{\tilde{x}} & \boldsymbol{e}_{\tilde{y}}\end{bmatrix}\begin{bmatrix}\tilde{x}_m\\\tilde{y}_m\end{bmatrix} \tag{27}$$

$$\boldsymbol{r}_n = \frac{1}{\sqrt{\lambda D}}\begin{bmatrix}\boldsymbol{e}_x^\top\\\boldsymbol{e}_y^\top\end{bmatrix}\begin{bmatrix}\boldsymbol{e}_{\tilde{x}'} & \boldsymbol{e}_{\tilde{y}'}\end{bmatrix}\begin{bmatrix}\tilde{x}'_n\\\tilde{y}'_n\end{bmatrix}, \tag{28}$$

which are conveniently dimensionless by virtue of the normalization by $\sqrt{\lambda D}$. The usefulness of this convention will be highlighted in Sec. V, where continuous apertures come into play.

B. IRS Channel

With all the arrays being planar, we can find orthonormal sets $\{\boldsymbol{e}_{\tilde{x}}, \boldsymbol{e}_{\tilde{y}}\}$, $\{\boldsymbol{e}'_{\tilde{x}}, \boldsymbol{e}'_{\tilde{y}}\}$, and $\{\boldsymbol{e}''_{\tilde{x}}, \boldsymbol{e}''_{\tilde{y}}\}$, and two-dimensional coordinates $\begin{bmatrix}\tilde{x}_m & \tilde{y}_m\end{bmatrix}^\top$, $\begin{bmatrix}\tilde{x}'_\ell & \tilde{y}'_\ell\end{bmatrix}^\top$, and $\begin{bmatrix}\tilde{x}''_n & \tilde{y}''_n\end{bmatrix}^\top$, satisfying

$$\begin{bmatrix}x_m\\y_m\\z_m\end{bmatrix} = -D_1\boldsymbol{e}_{z_1} + \begin{bmatrix}\boldsymbol{e}_{\tilde{x}} & \boldsymbol{e}_{\tilde{y}}\end{bmatrix}\begin{bmatrix}\tilde{x}_m\\\tilde{y}_m\end{bmatrix} \tag{29}$$

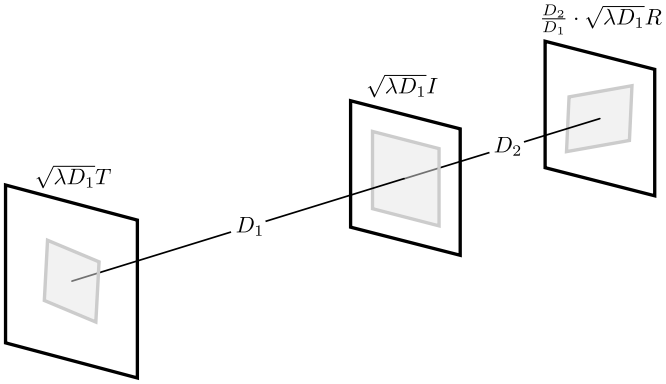

Fig. 6. Equivalent geometry.

$$\begin{bmatrix} x'_\ell \\ y'_\ell \\ z'_\ell \end{bmatrix} = \begin{bmatrix} \boldsymbol{e}_{\tilde{x}'} & \boldsymbol{e}_{\tilde{y}'} \end{bmatrix} \begin{bmatrix} \tilde{x}'_\ell \\ \tilde{y}'_\ell \end{bmatrix} \tag{30}$$

$$\begin{bmatrix} x''_n \\ y''_n \\ z''_n \end{bmatrix} = D_2 \boldsymbol{e}_{z_2} + \begin{bmatrix} \boldsymbol{e}_{\tilde{x}''} & \boldsymbol{e}_{\tilde{y}''} \end{bmatrix} \begin{bmatrix} \tilde{x}''_n \\ \tilde{y}''_n \end{bmatrix} \tag{31}$$

similarly to the point-to-point channel. Plugging them into (22) and (23),

$$[\boldsymbol{H}_1]_{\ell,m} = \exp\Bigg(j2\pi \Bigg(\frac{1}{\sqrt{\lambda D_1}} \begin{bmatrix} \boldsymbol{e}_{x_1}^\top \\ \boldsymbol{e}_{y_1}^\top \end{bmatrix} \begin{bmatrix} \boldsymbol{e}_{\tilde{x}'} & \boldsymbol{e}_{\tilde{y}'} \end{bmatrix} \begin{bmatrix} \tilde{x}'_\ell \\ \tilde{y}'_\ell \end{bmatrix} \cdot \frac{1}{\sqrt{\lambda D_1}} \begin{bmatrix} \boldsymbol{e}_{x_1}^\top \\ \boldsymbol{e}_{y_1}^\top \end{bmatrix} \begin{bmatrix} \boldsymbol{e}_{\tilde{x}} & \boldsymbol{e}_{\tilde{y}} \end{bmatrix} \begin{bmatrix} \tilde{x}_m \\ \tilde{y}_m \end{bmatrix} \Bigg) \Bigg) \tag{32}$$

$$[\boldsymbol{H}_2]_{n,\ell} = \exp\Bigg(j2\pi \Bigg(\frac{1}{\sqrt{\lambda D_2}} \begin{bmatrix} \boldsymbol{e}_{x_2}^\top \\ \boldsymbol{e}_{y_2}^\top \end{bmatrix} \begin{bmatrix} \boldsymbol{e}_{\tilde{x}''} & \boldsymbol{e}_{\tilde{y}''} \end{bmatrix} \begin{bmatrix} \tilde{x}''_n \\ \tilde{y}''_n \end{bmatrix} \cdot \frac{1}{\sqrt{\lambda D_2}} \begin{bmatrix} \boldsymbol{e}_{x_2}^\top \\ \boldsymbol{e}_{y_2}^\top \end{bmatrix} \begin{bmatrix} \boldsymbol{e}_{\tilde{x}'} & \boldsymbol{e}_{\tilde{y}'} \end{bmatrix} \begin{bmatrix} \tilde{x}'_\ell \\ \tilde{y}'_\ell \end{bmatrix} \Bigg) \Bigg), \tag{33}$$

which can be reduced to

$$[\boldsymbol{H}_1]_{\ell,m} = e^{j2\pi(\boldsymbol{i}_\ell \cdot \boldsymbol{t}_m)} \qquad [\boldsymbol{H}_2]_{n,\ell} = e^{j2\pi(\boldsymbol{r}_n \cdot \boldsymbol{i}_\ell)} \tag{34}$$

with

$$\boldsymbol{t}_m = \frac{1}{\sqrt{\lambda D_1}} \begin{bmatrix} \boldsymbol{e}_{\tilde{x}'}^\top \\ \boldsymbol{e}_{\tilde{y}'}^\top \end{bmatrix} (\boldsymbol{I} - \boldsymbol{e}_{z_1} \boldsymbol{e}_{z_1}^\top) \begin{bmatrix} \boldsymbol{e}_{\tilde{x}} & \boldsymbol{e}_{\tilde{y}} \end{bmatrix} \begin{bmatrix} \tilde{x}_m \\ \tilde{y}_m \end{bmatrix} \tag{35}$$

$$\boldsymbol{i}_\ell = \frac{1}{\sqrt{\lambda D_1}} \begin{bmatrix} \tilde{x}'_\ell \\ \tilde{y}'_\ell \end{bmatrix} \tag{36}$$

$$\boldsymbol{r}_n = \frac{D_1}{D_2} \cdot \frac{1}{\sqrt{\lambda D_1}} \begin{bmatrix} \boldsymbol{e}_{\tilde{x}'}^\top \\ \boldsymbol{e}_{\tilde{y}'}^\top \end{bmatrix} (\boldsymbol{I} - \boldsymbol{e}_{z_2} \boldsymbol{e}_{z_2}^\top) \begin{bmatrix} \boldsymbol{e}_{\tilde{x}''} & \boldsymbol{e}_{\tilde{y}''} \end{bmatrix} \begin{bmatrix} \tilde{x}''_n \\ \tilde{y}''_n \end{bmatrix}. \tag{37}$$

These equations imply that every orientation can be equivalently regarded as broadside, with the roles of transmitter and receiver played by their appropriate projections while the IRS is not subject to projection. Precisely, the channels in (34) are identical to the channels spawned by antennas and IRS elements having coordinates

$$\begin{bmatrix} x_m \\ y_m \\ z_m \end{bmatrix} = \begin{bmatrix} \sqrt{\lambda D_1} \boldsymbol{t}_m \\ -D_1 \end{bmatrix} \tag{38}$$

$$\begin{bmatrix} x'_\ell \\ y'_\ell \\ z'_\ell \end{bmatrix} = \begin{bmatrix} \sqrt{\lambda D_1} \boldsymbol{i}_\ell \\ 0 \end{bmatrix} \tag{39}$$

$$\begin{bmatrix} x''_n \\ y''_n \\ z''_n \end{bmatrix} = \begin{bmatrix} \frac{D_2}{D_1} \cdot \sqrt{\lambda D_1} \boldsymbol{r}_n \\ D_2 \end{bmatrix} \tag{40}$$

by virtue of the point-to-point result in Sec. IV-A. Fig. 6 depicts this broadside geometry where T, I, and R are continuous counterparts of $\{\boldsymbol{t}_m\}$, $\{\boldsymbol{i}_\ell\}$, and $\{\boldsymbol{r}_n\}$, to be introduced in Sec. VI.

The above equivalent broadside geometry enables sidestepping the existence of distinct IRS projections for the transmitter-IRS and IRS-receiver links (see Fig. 2) if transmitter and receiver are projected on planes orthogonal to those respective links.

C. UPAs

To make things precise for UPAs, consider the transmitter specifically. Choosing as principal axes $\boldsymbol{e}_{\tilde{x}}$ and $\boldsymbol{e}_{\tilde{y}}$ is convenient for UPAs. Then, the $N_{\mathrm{t},x} \times N_{\mathrm{t},y}$ transmit UPA having a footprint of $L_{\mathrm{t},x} \times L_{\mathrm{t},y}$, measured in meters, has the antennas whose coordinates are (41) where $d_{\mathrm{t},x} = \frac{L_{\mathrm{t},x}}{N_x}$ and $d_{\mathrm{t},y} = \frac{L_y}{N_y}$. The receiver and IRS can be similarly described.

V. Continuous-Aperture Representation

Explaining the rationale behind the optimality of the proposed phase shifts calls for an analytical tool, the continuous-aperture representation, presented herein for a point-to-point channel and which may be of independent value. The arrays are represented by a continuous aperture having infinitely many infinitesimal antennas, a representation that becomes progressively accurate as the antenna spacings shrink. The communication via continuous apertures is actually a notion of its own, namely holographic MIMO [48], [49]. Here, though, we invoke the continuous-aperture model as a proxy for analysis rather an exact physical representation, and the interest lies in applying the findings obtained with this model to practically relevant array densities.

A. Mathematical Preliminaries

Moving from the discrete to the continuous realm brings about mathematical complications. Objects may be pathological, and properties taken for granted in finite-dimensional spaces need not hold. Restricting our attention to well-behaved spaces, objects are confined to square-integrable functions and Hilbert-Schmidt operators, which are the analogues of vectors and matrices in the discrete world.

We say that $f : \mathbb{R}^d \to \mathbb{C}$ is square-integrable if and only if $\int |f(x)|^2 dx < \infty$. The set of square-integrable functions is written as $L^2(\mathbb{R}^d)$. We say that $\mathcal{L} : L^2(\mathbb{R}^d) \to L^2(\mathbb{R}^d)$ is Hilbert-Schmidt if and only if its explicit mapping rule is $(\mathcal{L}f)(x) = \int k(x,y) f(y) dy$ with square-integrable kernel $k : \mathbb{R}^d \times \mathbb{R}^d \to \mathbb{C}$, i.e., $\iint |k(x,y)|^2 dx\, dy < \infty$. Given the Hilbert-Schmidt operator $\mathcal{L}$, $\mathcal{L}f$ is well-defined almost everywhere and is again square-integrable [50, Thm 8.2.1].

To assist the reader, integral operators and their matrix counterparts are listed in Table I. The vector $\boldsymbol{x} \in \mathbb{C}^q$ and matrix $\boldsymbol{A} \in \mathbb{C}^{p \times q}$ can be identified, respectively, with the function $i \mapsto [\boldsymbol{x}]_i$ (whose domain is $\{1, 2, \ldots, q\}$) and with

$$\left\{\begin{bmatrix}\tilde{x}_m\\ \tilde{y}_m\end{bmatrix} \,|\, m=1,\dots,N_{\mathrm{t}}\right\} = \begin{Bmatrix} d_{\mathrm{t},x}\mathbb{Z} & \text{for odd } N_{\mathrm{t},x} \\ d_{\mathrm{t},x}\big(\mathbb{Z}-\frac{1}{2}\big) & \text{for even } N_{\mathrm{t},x}\end{Bmatrix} \times \begin{Bmatrix} d_{\mathrm{t},y}\mathbb{Z} & \text{for odd } N_{\mathrm{t},y} \\ d_{\mathrm{t},y}\big(\mathbb{Z}-\frac{1}{2}\big) & \text{for even } N_{\mathrm{t},y}\end{Bmatrix} \cap \left(L_{\mathrm{t},x}\left[-\frac{1}{2},\frac{1}{2}\right]\times L_{\mathrm{t},y}\left[-\frac{1}{2},\frac{1}{2}\right]\right) \tag{41}$$

TABLE I
LIST OF ANALOGIES.

		Discrete		Continuous
Object	vector	$\boldsymbol{x}\in\mathbb{C}^q$	function	$f(y)\in L^2(\mathbb{R}^d)$
	matrix	$\boldsymbol{A}\in\mathbb{C}^{p\times q}$	kernel	$k(x,y)\in L^2(\mathbb{R}^d\times\mathbb{R}^d)$
Operation	matrix-vector product	$[\boldsymbol{A}\boldsymbol{x}]_m=\sum_n[\boldsymbol{A}]_{m,n}[\boldsymbol{x}]_n$	-	$(\mathcal{L}f)(x)=\int k(x,y)f(y)dy$
	matrix-matrix product	$[\boldsymbol{A}_1\boldsymbol{A}_2]_{m,n}=\sum_\ell[\boldsymbol{A}_1]_{m,\ell}[\boldsymbol{A}_2]_{\ell,n}$	composition	$(\mathcal{L}_1\mathcal{L}_2f)(x)=\int(\int k_1(x,z)k_2(z,y)dz)f(y)dy$
	conjugate transpose	$[\boldsymbol{A}^*]_{m,n}=[\boldsymbol{A}]_{n,m}$	adjoint	$(\mathcal{L}^*f)(x)=\int\overline{k(y,x)}f(y)dy$
	inner product	$\boldsymbol{x}_1^*\boldsymbol{x}_2$	inner product	$\langle f_1,f_2\rangle=\int f_1(x)\overline{f_2(x)}dy$
Property	self-adjoint	$\boldsymbol{A}=\boldsymbol{A}^*$	self-adjoint	$\mathcal{L}=\mathcal{L}^*$
	positive-semidefinite	$\boldsymbol{x}^*\boldsymbol{A}\boldsymbol{x}\geq 0,\forall\boldsymbol{x}\in\mathbb{C}^q$	positive-semidefinite	$\langle\mathcal{L}f,f\rangle\geq 0,\forall f\in L^2(\mathbb{R}^d)$
Norm	Euclidean norm	$\|\boldsymbol{x}\|=(\boldsymbol{x}^*\boldsymbol{x})^{\frac{1}{2}}$	Euclidean norm	$\|f\|=\langle f,f\rangle^{\frac{1}{2}}$
	operator norm	$\|\boldsymbol{A}\|_2=\sup_{\|\boldsymbol{x}\|=1}\|\boldsymbol{A}\boldsymbol{x}\|$	operator norm	$\|\mathcal{L}\|_{\mathrm{op}}=\sup_{\|\boldsymbol{x}\|=1}\|\mathcal{L}f\|$
Spectral theory	eigenvalue	$\boldsymbol{A}\boldsymbol{x}=\lambda\boldsymbol{x}$	eigenvalue	$\mathcal{L}f=\lambda f$
	singular value	$\boldsymbol{A}\boldsymbol{v}=\sigma\boldsymbol{u}$	singular value	$\mathcal{L}v=\sigma u$

the linear mapping $\boldsymbol{x}\mapsto\boldsymbol{A}\boldsymbol{x}$. Armed with the notions in Table I, results that are instrumental to the ensuing analysis are put forth next, with the overline notation denoting complex conjugation.

Theorem 1 (Spectral theorem [50, Thm 7.8.1]): Let $\mathcal{L}: L^2(\mathbb{R}^d)\to L^2(\mathbb{R}^d)$ be a self-adjoint Hilbert-Schmidt operator with kernel k. There exists a real sequence $\{\lambda_n\}_{n\in\mathbb{N}}$ converging to zero and an orthonormal basis $\{e_n\}_{n\in\mathbb{N}}$ such that

$$\mathcal{L}f=\sum_{n=1}^{\infty}\lambda_n\langle f,e_n\rangle\,e_n \tag{42}$$

for all $f\in L^2(\mathbb{R}^d)$. In terms of kernel,

$$k(x,y)=\sum_{n=1}^{\infty}\lambda_n\,e_n(x)\,\overline{e_n(y)}. \tag{43}$$

The convergence of (42) and (43) are in the Euclidean norms on $L^2(\mathbb{R}^d)$ and $L^2(\mathbb{R}^d\times\mathbb{R}^d)$, respectively. Each λ_n is an eigenvalue of $\mathcal{L}$ and e_n is the corresponding eigenvector.

Theorem 2 (Singular value decomposition [50, Thm 7.9.3]): Let $\mathcal{L}: L^2(\mathbb{R}^d)\to L^2(\mathbb{R}^d)$ be a Hilbert-Schmidt operator with kernel k. There exists a nonnegative decreasing sequence $\{\sigma_n\}_{n\in\mathbb{N}}$, termed singular value, and orthonormal sequences $\{u_n\}_{n\in\mathbb{N}}$ and $\{v_n\}_{n\in\mathbb{N}}$ satisfying

$$\mathcal{L}f=\sum_{n=1}^{\infty}\sigma_n\langle f,v_n\rangle\,u_n \tag{44}$$

for all $f\in L^2(\mathbb{R}^d)$. In terms of kernel,

$$k(x,y)=\sum_{n=1}^{\infty}\sigma_n\,u_n(x)\,\overline{v_n(y)}. \tag{45}$$

Singular value and eigenvalue are related via

$$\sigma_n^2(\mathcal{L})=\lambda_n(\mathcal{L}^*\mathcal{L})=\lambda_n(\mathcal{L}\mathcal{L}^*) \tag{46}$$

and $\lambda_n(\mathcal{L})=\sigma_n(\mathcal{L})$ for any positive semidefinite operator $\mathcal{L}$. In addition, from (45),

$$\sum_{n=1}^{\infty}\sigma_n^2(\mathcal{L})=\iint|k(x,y)|^2\,dx\,dy. \tag{47}$$

For the sake of convenience, we let $\sigma_n(\boldsymbol{A})=0$ for $n>\min(p,q)$ and define the vector $\boldsymbol{\sigma}=(\sigma_1,\sigma_2,\dots)$. The singular values and eigenvalues are always arranged in descending order.

B. Continuous Counterpart of a Point-to-Point Channel

The continuous counterparts of transmit and receive UPAs, in $\tilde{x}\tilde{y}$ and $\tilde{x}'\tilde{y}'$ coordinates, are $L_{\mathrm{t},x}\left[-\frac{1}{2},\frac{1}{2}\right]\times L_{\mathrm{t},y}\left[-\frac{1}{2},\frac{1}{2}\right]$ and $L_{\mathrm{r},x}\left[-\frac{1}{2},\frac{1}{2}\right]\times L_{\mathrm{r},y}\left[-\frac{1}{2},\frac{1}{2}\right]$, respectively. In turn, from (27) and (28), those of $\{\boldsymbol{t}_m\}$ and $\{\boldsymbol{r}_n\}$ in xy coordinates are the dimensionless parallelograms

$$T=\frac{1}{\sqrt{\lambda D}}\begin{bmatrix}\boldsymbol{e}_x^\top\\ \boldsymbol{e}_y^\top\end{bmatrix}\begin{bmatrix}\boldsymbol{e}_{\tilde{x}} & \boldsymbol{e}_{\tilde{y}}\end{bmatrix}\left(L_{\mathrm{t},x}\left[-\frac{1}{2},\frac{1}{2}\right]\times L_{\mathrm{t},y}\left[-\frac{1}{2},\frac{1}{2}\right]\right) \tag{48}$$

$$R=\frac{1}{\sqrt{\lambda D}}\begin{bmatrix}\boldsymbol{e}_x^\top\\ \boldsymbol{e}_y^\top\end{bmatrix}\begin{bmatrix}\boldsymbol{e}_{\tilde{x}'} & \boldsymbol{e}_{\tilde{y}'}\end{bmatrix}\left(L_{\mathrm{r},x}\left[-\frac{1}{2},\frac{1}{2}\right]\times L_{\mathrm{r},y}\left[-\frac{1}{2},\frac{1}{2}\right]\right). \tag{49}$$

Although the interest is on parallelograms, arbitrary measurable sets T and R are considered. The continuous analogue of (26) is an integral operator $\mathcal{H}_{R,T}: L^2(\mathbb{R}^2)\to L^2(\mathbb{R}^2)$ defined by

$$(\mathcal{H}_{R,T}s)(\boldsymbol{r})=\int h_{R,T}(\boldsymbol{r},\boldsymbol{t})\,s(\boldsymbol{t})\,d\boldsymbol{t} \tag{50}$$

where $h_{R,T}(\boldsymbol{r},\boldsymbol{t})=\mathbf{1}_R(\boldsymbol{r})\,e^{j2\pi(\boldsymbol{t}\cdot\boldsymbol{r})}\,\mathbf{1}_T(\boldsymbol{t})$; henceforth, except where confusion may arise, the subscripts R,T are dropped. Note the relation $[\boldsymbol{H}]_{n,m}=h(\boldsymbol{r}_n,\boldsymbol{t}_m)$. We can decompose the channel as

$$\mathcal{H}=\mathbf{1}_R\,\mathcal{F}^{-1}\,\mathbf{1}_T \tag{51}$$

where $(\mathbf{1}_T s)(\boldsymbol{t}) = \mathbf{1}_T(\boldsymbol{t}) s(\boldsymbol{t})$ and $(\mathbf{1}_R s)(\boldsymbol{r}) = \mathbf{1}_R(\boldsymbol{r}) s(\boldsymbol{r})$ are projections, and $(\mathcal{F}^{-1} s)(\boldsymbol{t}) = \int s(\boldsymbol{r})\, e^{\jmath 2\pi (\boldsymbol{t}\cdot\boldsymbol{r})}\, d\boldsymbol{r}$ is the two-dimensional inverse Fourier transform, a unitary operator by virtue of Parseval's identity. This simple representation basically follows from the normalization in (48) and (49). From the representation (51), whose operations do not increase the norm,

$$\sigma_1 = \|\mathcal{H}\|_{\mathrm{op}} = \sup_{\|s\|=1} \|\mathbf{1}_R \mathcal{F}^{-1} \mathbf{1}_T s\| \le \sup_{\|s\|=1} \|s\| = 1. \quad (52)$$

What follows is $\sigma_n \le 1$ for all n, a boundedness that plays an important role in Sec. V-D.

There is also the invariance property (verifiable via change of variables) that, if T and R become $\boldsymbol{A}T$ and $\boldsymbol{A}^{-T}R$, the singular values are unchanged. This amounts to a simultaneous expansion of one array and shrinking of the other array, with identical factors.

C. Singular Value Relation

Let us now address the sense in which the continuous channel representation in (51) approximates the actual channel in (26). Being interested in the capacity, singular values are of great importance and thus we proceed to establish the relation between the singular values of $\boldsymbol{H}$ and $\mathcal{H}$. To this end, let us first discretize (50) by means of the Riemann sum approximation

$$(\mathcal{H}s)(\boldsymbol{r}_n) = \int h(\boldsymbol{r}_n, \boldsymbol{t})\, s(\boldsymbol{t})\, d\boldsymbol{t} \quad (53)$$

$$\approx \frac{\mathsf{area}(T)}{N_{\mathrm{t}}} [\boldsymbol{H}\boldsymbol{s}]_n, \quad (54)$$

where $[\boldsymbol{s}]_m = s(\boldsymbol{t}_m)$. Here, $\mathsf{area}(\cdot)$ denotes the Lebesgue measure on $\mathbb{R}^2$, and we note that all quantities of the form $\mathsf{area}(\cdot)$ are dimensionless owing to the normalization. (Recall the normalization by $\sqrt{\lambda D}$ in the definition of T and R in (48) and (49)).

Comparing it with the discretization of a singular value decomposition of $\mathcal{H}$, namely $\mathcal{H}s = \sum_{k=1}^{\infty} \sigma_k \langle s, v_k \rangle\, u_k$,

$$(\mathcal{H}s)(\boldsymbol{r}_n) = \sum_{k=1}^{\infty} \sigma_k \left(\int_T s(\boldsymbol{t}) \overline{v_k(\boldsymbol{t})} d\boldsymbol{t} \right) u_k(\boldsymbol{r}_n) \quad (55)$$

$$\approx \sum_{k=1}^{\infty} \sigma_k \left(\frac{\mathsf{area}(T)}{N_{\mathrm{t}}} \sum_m s(\boldsymbol{t}_m) \overline{v_k(\boldsymbol{t}_m)} \right) u_k(\boldsymbol{r}_n)$$

and, after factoring out the common term,

$$[\boldsymbol{H}\boldsymbol{s}]_n \approx \sum_{k=1}^{\infty} \sigma_k \left(\sum_m s(\boldsymbol{t}_m) \overline{v_k(\boldsymbol{t}_m)} \right) u_k(\boldsymbol{r}_n) \quad (56)$$

$$= \sum_{k=1}^{\infty} \sqrt{\frac{N_{\mathrm{t}} N_{\mathrm{r}}}{\mathsf{area}(T)\mathsf{area}(R)}}\, \sigma_k [\boldsymbol{u}_k]_n \boldsymbol{v}_k^* \boldsymbol{s} \quad (57)$$

$$\approx \sum_{k=1}^{\min(N_{\mathrm{t}}, N_{\mathrm{r}})} \sqrt{\frac{N_{\mathrm{t}} N_{\mathrm{r}}}{\mathsf{area}(T)\mathsf{area}(R)}}\, \sigma_k [\boldsymbol{u}_k]_n \boldsymbol{v}_k^* \boldsymbol{s} \quad (58)$$

where

$$[\boldsymbol{u}_k]_n = \sqrt{\frac{\mathsf{area}(R)}{N_{\mathrm{r}}}} u_k(\boldsymbol{r}_n) \qquad [\boldsymbol{v}_k]_m = \sqrt{\frac{\mathsf{area}(T)}{N_{\mathrm{t}}}} v_k(\boldsymbol{t}_m).$$

The multiplicative constants have been introduced to properly normalize the singular vectors, that is, $\|\boldsymbol{u}_k\|^2 \approx \|u_k\|^2 = 1$ and $\|\boldsymbol{v}_k\|^2 \approx \|v_k\|^2 = 1$. This discretization, in turn, suggests that

$$\boldsymbol{H} \approx \sum_{k=1}^{\min(N_{\mathrm{t}}, N_{\mathrm{r}})} \sqrt{\frac{N_{\mathrm{t}} N_{\mathrm{r}}}{\mathsf{area}(T)\mathsf{area}(R)}}\, \sigma_k \boldsymbol{u}_k \boldsymbol{v}_k^*. \quad (59)$$

Since the right-hand side can be regarded as a singular value decomposition with singular values $(\frac{N_{\mathrm{t}} N_{\mathrm{r}}}{\mathsf{area}(T)\mathsf{area}(R)})^{1/2} \sigma_k$, left singular vectors $\boldsymbol{u}_k$, and right singular vectors $\boldsymbol{v}_k$,

$$\sigma_k(\boldsymbol{H}) \approx \sqrt{\frac{N_{\mathrm{t}} N_{\mathrm{r}}}{\mathsf{area}(T)\mathsf{area}(R)}}\, \sigma_k(\mathcal{H}). \quad (60)$$

This approximation sharpens as the number of antennas increases, precisely

$$\left\| \boldsymbol{\sigma}(\mathcal{H}) - \sqrt{\frac{\mathsf{area}(T)\mathsf{area}(R)}{N_{\mathrm{t}} N_{\mathrm{r}}}}\, \boldsymbol{\sigma}(\boldsymbol{H}) \right\| = \mathcal{O}(N^{-1}), \quad (61)$$

where $N_{\mathrm{t},x}, N_{\mathrm{t},y}, N_{\mathrm{r},x}, N_{\mathrm{r},y}$ are proportional to N with the footprints fixed (see App. D). Note that (60) is consistent with $\sum_n \sigma_n^2(\boldsymbol{H}) = N_{\mathrm{t}} N_{\mathrm{r}}$ and $\sum_n \sigma_n^2(\mathcal{H}) = \mathsf{area}(T)\mathsf{area}(R)$.

D. Asymptotic Polarization of Singular Values

To gauge the asymptotic behavior of the singular values, we consider a receive aperture rR with varying expansion r while leaving the transmit aperture T unchanged. By virtue of the invariance property, this is equivalent to expanding T by r_1 and R by r_2 with $r_1 r_2 = r$.

Our interest is on the family of linear operators $\mathcal{H}_{rR,T} : L^2(\mathbb{R}^2) \to L^2(\mathbb{R}^2)$ indexed by r, and its asymptotic behavior as $r \to \infty$. We define

$$\mathsf{DOF} = \mathsf{area}(T)\mathsf{area}(R), \quad (62)$$

a notation whose rationale will become clear. From [51, Lemma 1], we have that

$$\sum_n \lambda_n(\mathcal{H}_{rR,T} \mathcal{H}_{rR,T}^*) = r^2 \mathsf{DOF} \quad (63)$$

and

$$\sum_n \lambda_n^2(\mathcal{H}_{rR,T} \mathcal{H}_{rR,T}^*) = r^2 \mathsf{DOF} - o(r^2), \quad (64)$$

and thus

$$|\{\lambda_n(\mathcal{H}_{rR,T} \mathcal{H}_{rR,T}^*) > \epsilon\}| = r^2 \mathsf{DOF} - o(r^2) \quad (65)$$

for any $0 < \epsilon < 1$ [51, Thm 1]. Put into words, $\mathcal{H}$ has approximately DOF significant singular values near one. This generalizes the result for broadside rectangular arrays in [23] and, combined with (60), leads to

$$\boldsymbol{\sigma}(\boldsymbol{H}) \approx \sqrt{\frac{N_{\mathrm{t}} N_{\mathrm{r}}}{\mathsf{DOF}}}\, \boldsymbol{\sigma}(\mathcal{H}) \approx \sqrt{\frac{N_{\mathrm{t}} N_{\mathrm{r}}}{\mathsf{DOF}}}\, (\underbrace{1, \ldots, 1}_{\mathsf{DOF}}, 0, \ldots), \quad (66)$$

which indicates that the product of normalized footprints determines the DOF while the antenna density determines the power gain. (Recall that each array's footprint is normalized by $\sqrt{\lambda D}$ per dimension, hence the DOF additionally scale with $1/\lambda^2 D^2$.)

The singular value polarization in (66) holds for apertures that are minimally large, yet not large enough to violate

the small-aperture approximation that underpins (7). As shall be seen in Sec. VII, this encompasses a broad range of situations of interest for IRS channels.[1] In the sequel, the term "asymptotic" refers to the singular value polarization holding.

VI. Asymptotic Behavior of Proposed Phase Shift

Equipped with the results in the previous section, we next characterize the behavior of $\boldsymbol{\sigma}(\boldsymbol{H}_{\mathsf{eff}})$ for the proposed phase shift and contrast it with that of $\boldsymbol{\sigma}(\boldsymbol{H}_2) \circ \boldsymbol{\sigma}(\boldsymbol{H}_1)$, which embodies the capacity upper bound. These behaviors are shown to be asymptotically identical when a certain condition is met, hence the proposed phase shift is asymptotically optimum under such condition.

A. Continuous Representation and Singular Value Relation for IRS Channels

Similar to the point-to-point case, the continuous representation for IRS channels is

$$(\mathcal{H}_{I,T}s)(\boldsymbol{i}) = \int h_{I,T}(\boldsymbol{i},\boldsymbol{t})\, s(\boldsymbol{t})\, d\boldsymbol{t} \tag{67}$$

$$(\mathcal{H}_{R,I}s)(\boldsymbol{r}) = \int h_{R,I}(\boldsymbol{r},\boldsymbol{i})\, s(\boldsymbol{i})\, d\boldsymbol{i}, \tag{68}$$

where

$$T = \frac{1}{\sqrt{\lambda D_1}} \begin{bmatrix} \boldsymbol{e}_{\tilde{x}'}^\top \\ \boldsymbol{e}_{\tilde{y}'}^\top \end{bmatrix} (\boldsymbol{I} - \boldsymbol{e}_{z_1}\boldsymbol{e}_{z_1}^\top) \begin{bmatrix} \boldsymbol{e}_{\tilde{x}} & \boldsymbol{e}_{\tilde{y}} \end{bmatrix} \cdot \left(L_{\mathrm{t},x}\left[-\frac{1}{2},\frac{1}{2}\right] \times L_{\mathrm{t},y}\left[-\frac{1}{2},\frac{1}{2}\right] \right) \tag{69}$$

$$I = \frac{1}{\sqrt{\lambda D_1}} \left(L_{\mathrm{i},x}\left[-\frac{1}{2},\frac{1}{2}\right] \times L_{\mathrm{i},y}\left[-\frac{1}{2},\frac{1}{2}\right] \right) \tag{70}$$

$$R = \frac{D_1}{D_2} \cdot \frac{1}{\sqrt{\lambda D_1}} \begin{bmatrix} \boldsymbol{e}_{\tilde{x}'}^\top \\ \boldsymbol{e}_{\tilde{y}'}^\top \end{bmatrix} (\boldsymbol{I} - \boldsymbol{e}_{z_2}\boldsymbol{e}_{z_2}^\top) \begin{bmatrix} \boldsymbol{e}_{\tilde{x}''} & \boldsymbol{e}_{\tilde{y}''} \end{bmatrix} \cdot \left(L_{\mathrm{r},x}\left[-\frac{1}{2},\frac{1}{2}\right] \times L_{\mathrm{r},y}\left[-\frac{1}{2},\frac{1}{2}\right] \right). \tag{71}$$

Now, the operator of interest is $\mathcal{H}_{\mathsf{eff}} = \mathcal{H}_{R,I}\mathcal{H}_{I,T}$. Proceeding as in the point-to-point case,

$$\sigma_n(\boldsymbol{H}_{\mathsf{eff}}) \approx \frac{M}{\mathsf{area}(I)} \sqrt{\frac{N_{\mathrm{t}}N_{\mathrm{r}}}{\mathsf{area}(T)\mathsf{area}(R)}}\, \sigma_n(\mathcal{H}_{\mathsf{eff}}). \tag{72}$$

B. Asymptotic Polarization

To establish the asymptotic behavior of $\mathcal{H}_{\mathsf{eff}}$, we scale the IRS aperture by r, such that $\mathcal{H}_{\mathsf{eff}} = \mathcal{H}_{R,rI}\mathcal{H}_{rI,T}$, and investigate the asymptotic order of the sum and squared sum of the eigenvalues. Note, from $\|\mathcal{H}_{\mathsf{eff}}\|_{\mathrm{op}} \leq 1$, that $\lambda_n(\mathcal{H}_{\mathsf{eff}}\mathcal{H}_{\mathsf{eff}}^*) \leq 1$; this is as in the point-to-point case.

The sum of eigenvalues can be computed as

$$\sum_n \lambda_n(\mathcal{H}_{\mathsf{eff}}\mathcal{H}_{\mathsf{eff}}^*) = r^2\mathsf{DOF} + o(r^2), \tag{73}$$

where, here, $\mathsf{DOF} = \mathsf{area}(I)\mathsf{area}(T \cap (-R))$, with the negative sign arising because the signal is flipped. In turn,

$$\sum_n \lambda_n^2(\mathcal{H}_{\mathsf{eff}}\mathcal{H}_{\mathsf{eff}}^*) = r^2\mathsf{DOF} + o(r^2). \tag{74}$$

[1]This is not unlike the asymptotic analyses of MIMO that have been so instrumental to cast light on key behaviors: the arrays involved have to be large, yet not excessively large lest some of the models break down [52].

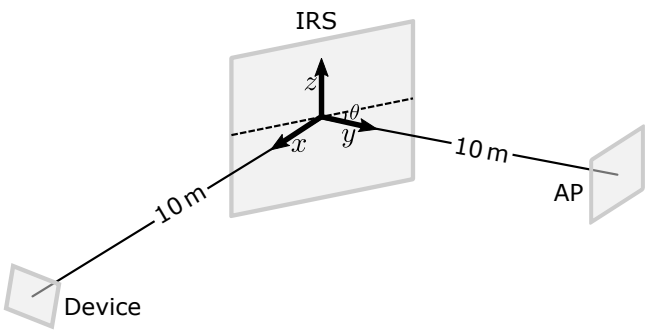

Fig. 7. Considered geometry for the numerical simulations. The AP is parallel to the xz-plane; other orientations would simply entail the appropriate projection.

The derivations of (73) and (74) are relegated to App. E. Together with boundedness, these relationships lead to the polarization of the eigenvalues (or concentration of spectrum)

$$|\{\lambda_n(\mathcal{H}_{\mathsf{eff}}\mathcal{H}_{\mathsf{eff}}^*) > \epsilon\}| = r^2\mathsf{DOF} - o(r^2) \tag{75}$$

for any $0 < \epsilon < 1$.

C. Achievable Spectral Efficiency vs Capacity Upper Bound

In the asymptotic regime, with the singular values being polarized,

$$\boldsymbol{\sigma}(\boldsymbol{H}_{\mathsf{eff}}) \approx \frac{M}{\mathsf{area}(I)} \sqrt{\frac{N_{\mathrm{t}}N_{\mathrm{r}}}{\mathsf{area}(T)\mathsf{area}(R)}} (\underbrace{1,\ldots,1}_{\mathsf{DOF}},0,\ldots) \tag{76}$$

and

$$\boldsymbol{\sigma}(\boldsymbol{H}_2) \circ \boldsymbol{\sigma}(\boldsymbol{H}_1) \approx \frac{M}{\mathsf{area}(I)} \sqrt{\frac{N_{\mathrm{t}}N_{\mathrm{r}}}{\mathsf{area}(T)\mathsf{area}(R)}} (\underbrace{1,\ldots,1}_{\mathsf{DOF}^{\mathsf{up}}},0,\ldots), \tag{77}$$

where $\mathsf{DOF}^{\mathsf{up}} = \mathsf{area}(I)\min\big(\mathsf{area}(T), \mathsf{area}(R)\big)$. (As shown in App. F, this DOF expression, derived under the broadside geometry in Fig. 6, is equivalent to (2), formulated under the geometry in Fig. 2.) Two key insights can be gleaned:

- The singular values in (76) and (77) are asymptotically identical if and only if $\mathsf{DOF} = \mathsf{DOF}^{\mathsf{up}}$, which we refer to as the asymptotic optimality condition. This is tantamount to $T \subset -R$ or $T \supset -R$, a condition that is graphically illustrated in Figs. 9a–9b.
- The DOF then grow in direct proportion with the IRS footprint, as opposed to being limited only by transmitter and receiver.

Having indoor scenarios in mind, the transmitter and receiver are hereafter embodied by an access point (AP) and a device, respectively. The next section examines how the proposed phase shift performs, with and without the asymptotic optimality condition being satisfied.

VII. Numerical Results and Observations

This section presents corroborating numerical evidence that the proposed phase shifts, despite originating from asymptotic insights, are effective even for small apertures. The exact

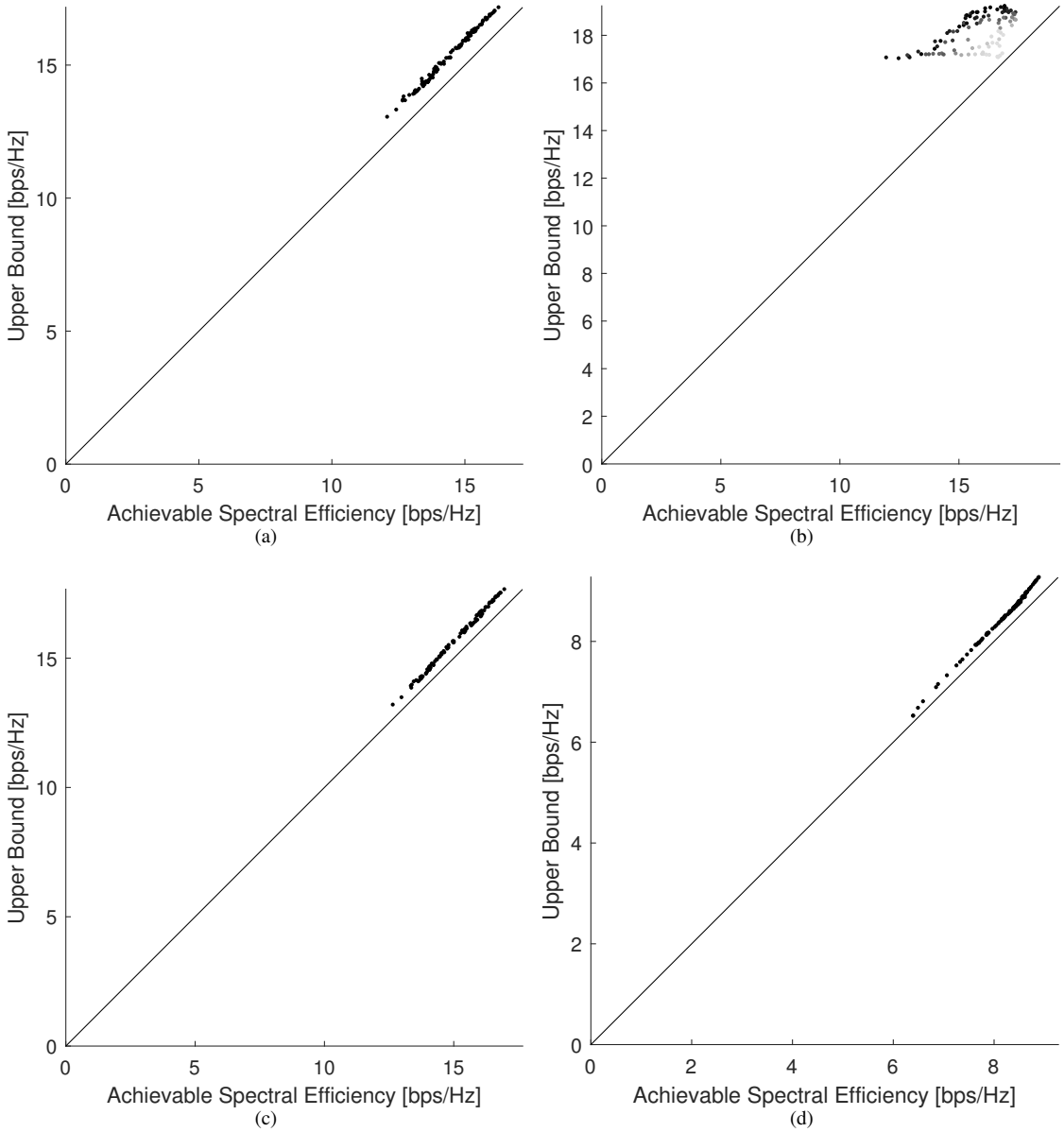

Fig. 8. Spectral efficiency achievable with the proposed phase shift vs the upper bound for various setups, with $P_{\mathrm{t}} = 10$ dBm. Each point represents the pair (achievable spectral efficiency, upper bound) for a realization of the device orientation. For Fig. 8b, the larger $\frac{\mathsf{DOF}}{\mathsf{DOF}^{\mathsf{up}}}$, the lighter the corresponding color.

channel model in (3) is used, without reliance on the small-aperture approximation. The simulation parameters are summarized in Table II. For each case labelled "random" in Table II, one hundred random orientations are generated. As the purpose of this randomization is generality, the differences in antenna directivity are not taken into account.

A. Proposed Phase Shift Quasi-Optimum when Asymptotic Optimality Condition Holds

For $\theta = 45°$, we have that

$$T = [-0.4\sin 45°, 0.4\sin 45°] \times [-0.4, 0.4]$$

$$R = \begin{bmatrix} \boldsymbol{e}_{\tilde{x}'}^{\top} \\ \boldsymbol{e}_{\tilde{y}'}^{\top} \end{bmatrix} \left(\boldsymbol{I} - \boldsymbol{e}_{z_2}\boldsymbol{e}_{z_2}^{\top}\right) \left[\boldsymbol{e}_{\tilde{x}''} \;\; \boldsymbol{e}_{\tilde{y}''}\right] \left([-0.2, 0.2] \times [-0.2, 0.2]\right).$$

To show that $T \supset -R$ for any orientation of the device, it is enough to check that the four vertices of $-R$ are contained in T. As

$$\left\| \begin{bmatrix} \boldsymbol{e}_{\tilde{x}'}^{\top} \\ \boldsymbol{e}_{\tilde{y}'}^{\top} \end{bmatrix} \left(\boldsymbol{I} - \boldsymbol{e}_{z_2}\boldsymbol{e}_{z_2}^{\top}\right) \left[\boldsymbol{e}_{\tilde{x}''} \;\; \boldsymbol{e}_{\tilde{y}''}\right] \begin{bmatrix} 0.2 \\ 0.2 \end{bmatrix} \right\| \leq \left\| \begin{bmatrix} 0.2 \\ 0.2 \end{bmatrix} \right\| \quad (78)$$

and similarly for other vertices, they are contained in T. Therefore, asymptotic optimality holds, $\mathsf{DOF} = \mathsf{DOF}^{\mathsf{up}}$. Fig. 8a shows how the achievable spectral efficiency indeed approaches the capacity upper bound very closely.

B. Proposed Phase Shift Satisfactory even when Asymptotic Optimality Condition does not Hold

For $\theta = 15°$, there are device orientations for which neither $T \subset -R$ nor $T \supset -R$ holds (see Fig. 9). Shown in Fig. 8b is how the achievable spectral efficiency then

TABLE II
SIMULATION PARAMETERS

G_{t} [dBi]	G_{IRS} [dBi]	G_{r} [dBi]	PL_1 [dB]	PL_2 [dB]
7	0	7	-95.0	-95.0
λ [m]	B [GHz]	N_0 [dBm/GHz]	$\frac{P_{\mathrm{t}}}{BN_0}$ [dB]	SNR [dB]
0.001	1	-74	P_{t} [dBm] $+ 74$	P_{t} [dBm] $- 116$

	IRS	AP 1	AP 2	Device 1	Device 2
Size [cm $\times$ cm]	40×40	8×8	16×16	4×4	1×4
Spacing [cm]	0.05	2	2	1	1
Dimensionality	800×800	4×4	8×8	4×4	1×4
# of elements	640000	16	64	16	4

Section	VII-A	VII-B	VII-C	VII-D	VII-E	VII-F
AP index	1	1	2	1	1	1
Device index	1	1	1	2	1	1
θ	45°	15°	45°	45°	45°/15°	45°
Device orientation	Random	Random	Random	Random	IRS	IRS

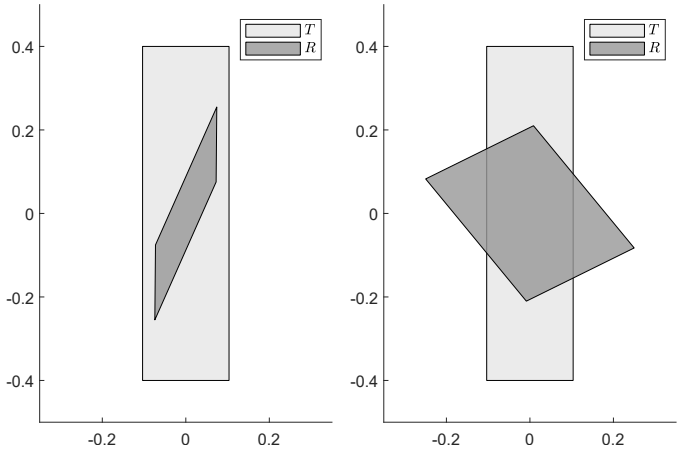

(a) The optimality condition is met. (b) The optimality condition is not met.

Fig. 9. T and R for distinct device orientations.

behaves. Remarkably, even in cases (dark points) in which the optimality condition decidedly does not hold, the performance is largely satisfactory. Moreover, some of the shortfall is caused by the upper bound itself being somewhat loose in this setup (refer to Sec. VII-E).

C. AP Footprint Comparable to Device Footprint Suffices

When the array at the AP is large enough that $T \supset -R$, we asymptotically have $\mathsf{DOF} = \mathsf{area}(I)\mathsf{area}(R)$ with a per-spatial-signal SNR of

$$\frac{M^2 N_{\mathrm{t}} N_{\mathrm{r}}}{(\mathsf{area}(I))^2 \mathsf{area}(T)\mathsf{area}(R)} \cdot \frac{\mathsf{SNR}}{\mathsf{area}(I)\mathsf{area}(R)}. \tag{79}$$

Expanding $\mathsf{area}(T)$ while keeping the antenna density $\frac{N_{\mathrm{t}}}{\mathsf{area}(T)}$ does change neither the DOF nor the per-signal SNR, hence there is no point in enlarging the AP footprint beyond some point. An AP comparable in size to the device is sufficient.

TABLE III
IRS AMPLITUDE-PHASE RESPONSE AT 1.95 THZ [56].

Index	000	001	010	011	100	101	110	111
Amplitude	0.662	0.692	0.667	0.647	0.649	0.664	0.664	0.708
Phase [°]	-144.6	-110.3	-73.7	-27.8	17.7	57.8	105.0	143.5

To validate this, for Fig. 8c the AP is enlarged to twice its size in both planar dimensions relative to Fig. 8a. The improvement is indeed small: the lower-left point is $(12.08, 13.06)$ in Fig. 8a and $(12.64, 13.21)$ in Fig. 8c.

D. Proposed Phase Shift Works Even for a ULA

Although the theory has been developed for planar arrays, the proposed phase shift performs remarkably well even if the device employs a ULA. Fig. 8d illustrates the performance when a four-antenna ULA is employed at the device.

E. Proposed Phase Shift Performs Comparably to Existing Optimization Algorithms

Let us now compare the proposed phase shift against [31, Alg. 1], implemented with 100 different initializations and 100 iterations per transmit power level. Since the ensuing alternating optimization would be unwieldy for $M = 640000$—the per-iteration complexity is at least $(3{N_{\mathrm{r}}}^3 + 2{N_{\mathrm{r}}}^2 N_{\mathrm{t}})M$, which would be about 13.1 billion operations for $M = 640000$—we reduce the IRS element spacing by a factor of 10 while leaving the footprint unchanged, i.e., $M = 6400$. As per (72), the SNR is compensated by a factor of 10^4.

Fig. 10 shows how the proposed solution, explicit and straightforward to implement, performs essentially identically to the iterative algorithm, which is extremely intensive computationally.

F. Proposed Phase Shift Is Robust to Practical Amplitude-Phase Dependences

The amplitudes of the IRS element responses, regarded as identical in our models as in much of the corresponding literature, actually exhibit some fluctuations. Moreover, these fluctuations are connected to the phase shifts, i.e., $|[\boldsymbol{\Phi}]_{\ell,\ell}|$ is coupled with $\angle[\boldsymbol{\Phi}]_{\ell,\ell}$ [53], [54]. These amplitude variations can be flattened with more sophisticated element designs in term of materials or geometry [55], [56]. For our purpose here, we adopt the graphene-based design in [56, Fig. 2], whose amplitude-phase response under normal incidence is reproduced in Table III.

Fig. 11 shows the performance of our phase shift solution when rounded to the coarse granularity afforded by Table III and subject to the amplitude variations therein. Remarkably, the loss with respect to having infinite phase resolution and no amplitude variations is very small.

VIII. CONCLUSION

This paper has presented an upper bound on the IRS channel capacity and an explicit solution for the IRS phase

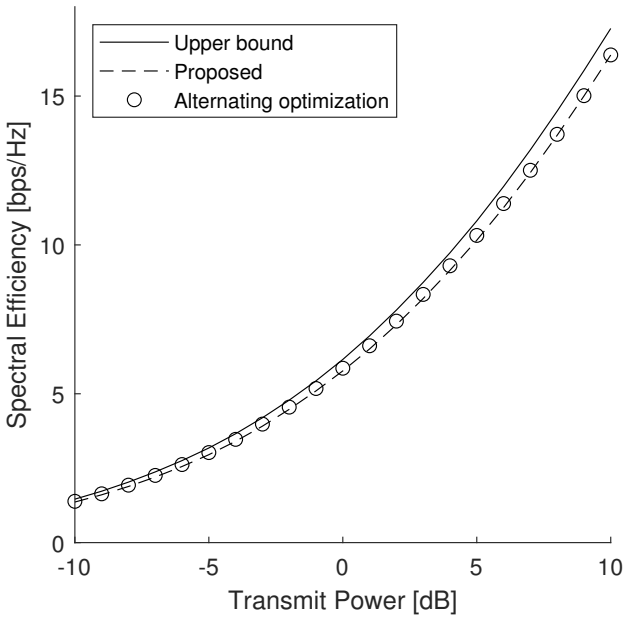

(a) $\theta = 45^\circ$.

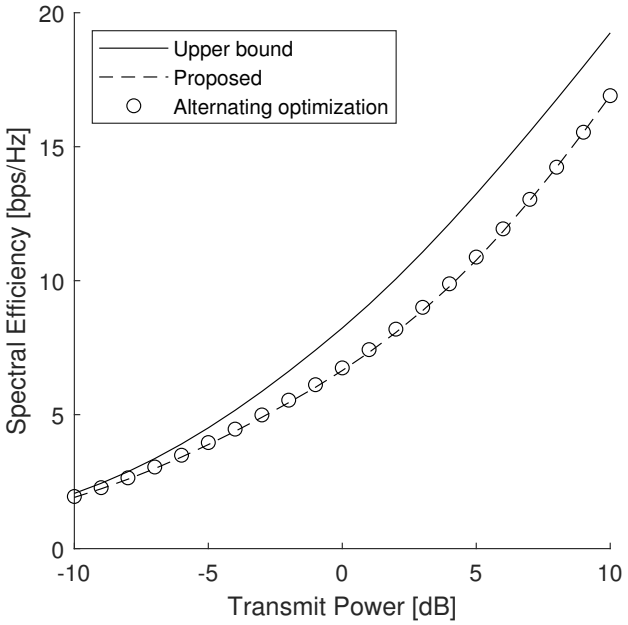

(b) $\theta = 15^\circ$.

Fig. 10. Proposed phase shift against alternating optimization.

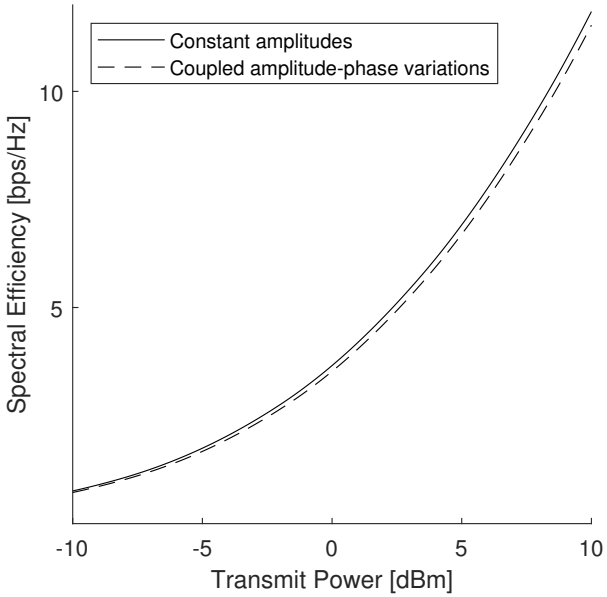

Fig. 11. Performance of the proposed phase shift under practical amplitude-phase dependences.

shifts that closely approaches such bound whenever a certain condition is satisfied. Crucially, the number of DOF then grows in proportion with the IRS aperture, as the solid angles subtended by that IRS aperture from both transmitter and receiver grow. The ensuing performance is excellent for a broad range of settings of interest, including cases in which the optimality condition is not met, and readers interested in further examples are referred to [57]. Potential directions for follow-up work are:

- To transcend the small-aperture approximation that underpins the results in their present form (see [36], [58]–[60] for incipient work on extremely large apertures) and to establish the IRS sizes up to which the behavior holds.
- To allow for an unblocked direct path from transmitter to receiver, as well as for multipath components.
- To incorporate channel estimation, extending as appropriate classical MIMO channel estimation schemes [61].

ACKNOWLEDGMENT

The authors thank Kasra Rouhi (Univ. of California at Irvine) for providing the simulation result in Table III and Andrea Pizzo (UPF) for helpful feedback and for the reference to [23]. The handling by the Associate Editor, and the feedback provided by the anonymous reviewers, are gratefully acknowledged.

APPENDIX A

The function

$$f : (x_1, \ldots, x_{N_{\mathsf{min}}}) \mapsto \max_{\sum_n p_n = \mathsf{SNR}} \sum_n \log_2\left(1 + e^{2x_m} p_n\right), \quad (80)$$

with $N_{\mathsf{min}} = \min(N_{\mathrm{t}}, N_{\mathrm{r}}, M)$, is symmetric and convex, hence Schur-convex [62, Prop. C.2]. Since $\boldsymbol{\sigma}(\boldsymbol{H}_2) \circ \boldsymbol{\sigma}(\boldsymbol{H}_1) = \boldsymbol{\sigma}(\boldsymbol{H}_2) \circ \boldsymbol{\sigma}(\boldsymbol{\Phi}\boldsymbol{H}_1)$ log-submajorizes $\boldsymbol{\sigma}(\boldsymbol{H}_2\boldsymbol{\Phi}\boldsymbol{H}_1)$ [63, Eq. (5.12)] and f is increasing with respect to each coordinate,

$$f(\log(\sigma_1(\boldsymbol{H}_2)\sigma_1(\boldsymbol{H}_1)), \ldots, \log(\sigma_{N_{\mathsf{min}}}(\boldsymbol{H}_2)\sigma_{N_{\mathsf{min}}}(\boldsymbol{H}_1))) \geq f(\log(\sigma_1(\boldsymbol{H}_2\boldsymbol{\Phi}\boldsymbol{H}_1)), \ldots, \log(\sigma_{N_{\mathsf{min}}}(\boldsymbol{H}_2\boldsymbol{\Phi}\boldsymbol{H}_1))). \quad (81)$$

With $\boldsymbol{\Phi} = \boldsymbol{V}_2\boldsymbol{U}_1^*$, we have $\boldsymbol{H}_2\boldsymbol{\Phi}\boldsymbol{H}_1 = \boldsymbol{U}_2\boldsymbol{\Sigma}_2\boldsymbol{\Sigma}_1\boldsymbol{V}_1^*$, implying that $\sigma_n(\boldsymbol{H}_1)\sigma_n(\boldsymbol{H}_2) = \sigma_n(\boldsymbol{H}_2\boldsymbol{\Phi}\boldsymbol{H}_1)$. Hence, (81) holds with equality.

$$\mathrm{Hess}(f(x',y')) = \frac{1}{((x_n''-x')^2+(y_n''-y')^2+(z_n'')^2)^{\frac{3}{2}}}\begin{bmatrix}-((y_n''-y')^2+(z_n'')^2) & (x_n''-x')(y_n''-y')\\ (x_n''-x')(y_n''-y') & -((x_n''-x')^2+(z_n'')^2)\end{bmatrix} + \frac{1}{((x_m-x')^2+(y_m-y')^2+z_m^2)^{\frac{3}{2}}}\begin{bmatrix}-((y_m-y')^2+z_m^2) & (x_m-x')(y_m-y')\\ (x_m-x')(y_m-y') & -((x_m-x')^2+z_m^2)\end{bmatrix}. \quad (86)$$

$$\mathrm{Hess}(f(x_0',y_0')) = \left(\frac{1}{z_n''}+\frac{1}{z_m}\right)\frac{z_n''+z_m}{((x_n''-x_m)^2+(y_n''-y_m)^2+(z_n''+z_m)^2)^{\frac{3}{2}}} \begin{bmatrix}-((y_n''-y_m)^2+(z_n''+z_m)^2) & (x_n''-x_m)(y_n''-y_m)\\ (x_n''-x_m)(y_n''-y_m) & -((x_n''-x_m)^2+(z_n''+z_m)^2)\end{bmatrix}. \quad (87)$$

APPENDIX B

Replacing the summation in (17) with integration, which is appropriate for sufficiently small spacings, we obtain $\iint g(x',y')e^{j\frac{2\pi}{\lambda}f(x',y')}dx'\,dy'$ with

$$f(x',y') = -\big(\sqrt{(x_n''-x')^2+(y_n''-y')^2+(z_n'')^2} + \sqrt{(x'-x_m)^2+(y'-y_m)^2+z_m^2}\big) \quad (82)$$

$$g(x',y') = \frac{1}{d_{\mathrm{i},x}d_{\mathrm{i},y}}\cdot\frac{D_1}{\sqrt{(x_n''-x')^2+(y_n''-y')^2+(z_n'')^2}} \cdot\frac{D_2}{\sqrt{(x'-x_m)^2+(y'-y_m)^2+z_m^2}} \cdot\mathbf{1}_{\left[-\frac{L_{\mathrm{i},x}}{2},\frac{L_{\mathrm{i},x}}{2}\right]\times\left[-\frac{L_{\mathrm{i},y}}{2},\frac{L_{\mathrm{i},y}}{2}\right]}(x',y'). \quad (83)$$

Applying the stationary phase approximation [64], for sufficiently small λ we can further approximate the integration with

$$\lambda\sum_{\substack{(x_0',y_o'):\\ \nabla f(x_0',y_o')=\mathbf{0}}} g(x_0',y_0')\,e^{j\frac{2\pi}{\lambda}f(x_0',y_0')}\left|\det\big(\mathrm{Hess}(f(x_0',y_0'))\big)\right|^{-\frac{1}{2}} \cdot e^{j\frac{\pi}{4}\,\mathrm{sgn}(\mathrm{Hess}(f(x_0',y_0')))} \quad (84)$$

where $\mathrm{Hess}(\cdot)$ denotes the Hessian of the argument and $\mathrm{sgn}(\mathrm{Hess}(\cdot))$ denotes its signature.

Let us find the stationary points characterizing the summands. From the observation that $-f(x',y')$ is the sum of two distances, one from (x_m,y_m,z_m) to $(x',y',0)$ and the other from $(x',y',0)$ to $(x_n'',y_n'',-z_n'')$, it is minimized only if $(x',y',0)$ is the point where the xy-plane and the line connecting (x_m,y_m,z_m) and $(x_n'',y_n'',-z_n'')$ intersect, i.e., the summation (84) is singleton:

$$(x_0',y_0') = \frac{z_n''}{z_n''+z_m}(x_m,y_m)+\frac{z_m}{z_n''+z_m}(x_n'',y_n''). \quad (85)$$

Straightforward calculation gives the Hessian in (86). Plugging (85) into (86), we obtain (87), hence

$$\det(\mathrm{Hess}(f(x_0',y_0'))) = \left(\frac{1}{z_n''}+\frac{1}{z_m}\right)^2\frac{(z_n''+z_m)^4}{((x_n''-x_m)^2+(y_n''-y_m)^2+(z_n''+z_m)^2)^2} \quad (88)$$

and $\mathrm{sgn}(\mathrm{Hess}(f(x_0',y_0'))) = -2$. Thus, (84) is reduced to

$$-\frac{j\lambda}{z_n''+z_m}\cdot\frac{D_1D_2}{d_{\mathrm{i},x}d_{\mathrm{i},y}}\cdot\mathbf{1}_{\left[-\frac{L_{\mathrm{i},x}}{2},\frac{L_{\mathrm{i},x}}{2}\right]\times\left[-\frac{L_{\mathrm{i},y}}{2},\frac{L_{\mathrm{i},y}}{2}\right]}(x_0',y_0') \cdot e^{-j\frac{2\pi}{\lambda}\sqrt{(x_n''-z_m)^2+(y_n''-y_m)^2+(z_n''+z_m)^2}}. \quad (89)$$

Note that (x_0',y_0') depends on (x_m,y_m,z_m) and (x_n'',y_n'',z_n'') although the notation conceals this dependence. Further imposing the small-aperture approximation on the amplitudes, $z_m\approx z\,\forall m$ and $z_n''\approx z''\,\forall n$, we finally obtain (18).

APPENDIX C

This appendix shows that the proposed phase shift performs optimally when both transmitter and receiver shrink into a point. Then, $\boldsymbol{H}_1$ and $\boldsymbol{H}_2$ are of rank-one, say $\boldsymbol{H}_1=\boldsymbol{u}_1\boldsymbol{v}_1^*$ and $\boldsymbol{H}_2=\boldsymbol{u}_2\boldsymbol{v}_2^*$. The highest spectral efficiency with a phase shift $\boldsymbol{\Phi}=\mathrm{diag}(e^{j\phi_1},\ldots,e^{j\phi_M})\in\mathbb{C}^{M\times M}$ is

$$C(\boldsymbol{\Phi}) = \max_{\sum_n p_n=\mathsf{SNR}}\sum_n\log_2\big(1+\sigma_n^2(\boldsymbol{H}_2\boldsymbol{\Phi}\boldsymbol{H}_1)\,p_n\big). \quad (90)$$

As $\boldsymbol{H}_2\boldsymbol{\Phi}\boldsymbol{H}_1$ is of rank-one,

$$C(\boldsymbol{\Phi}) = \log_2\big(1+\sigma_1^2(\boldsymbol{H}_2\boldsymbol{\Phi}\boldsymbol{H}_1)\,\mathsf{SNR}\big) \quad (91)$$

and

$$\sigma_1(\boldsymbol{H}_2\boldsymbol{\Phi}\boldsymbol{H}_1) = \|\boldsymbol{u}_2\boldsymbol{v}_2^*\boldsymbol{\Phi}\boldsymbol{u}_1\boldsymbol{v}_1^*\|_{\mathrm{F}} \quad (92)$$
$$= |\boldsymbol{v}_2^*\boldsymbol{\Phi}\boldsymbol{u}_1|\|\boldsymbol{u}_2\boldsymbol{v}_1^*\|_{\mathrm{F}} \quad (93)$$
$$= |\boldsymbol{v}_2^*\boldsymbol{\Phi}\boldsymbol{u}_1|\|\boldsymbol{u}_2\|\|\boldsymbol{v}_1\|. \quad (94)$$

Hence, the optimization of $\boldsymbol{\Phi}$ boils down to

$$\max_{\boldsymbol{\Phi}}|\boldsymbol{v}_2^*\boldsymbol{\Phi}\boldsymbol{u}_1| = \max_{\phi_1,\ldots,\phi_M}\left|\overline{[\boldsymbol{v}_2]_1}[\boldsymbol{u}_1]_1e^{j\phi_1}+\ldots+\overline{[\boldsymbol{v}_2]_M}[\boldsymbol{u}_1]_Me^{j\phi_M}\right| \quad (95)$$
$$= \left|\overline{[\boldsymbol{v}_2]_1}[\boldsymbol{u}_1]_1\right|+\ldots+\left|\overline{[\boldsymbol{v}_2]_M}[\boldsymbol{u}_1]_M\right|, \quad (96)$$

where the maximum is attained when coherently adding the summands [65, Lemma 1].

Let us apply this result to the channels in (12) and (13) when the transmit and receive arrays shrink into point sources at $-D_1\boldsymbol{e}_{z_1}$ and $D_2\boldsymbol{e}_{z_2}$, respectively. Then, (12) and (13) are reduced to (97) and (98), respectively, which can be written as $\boldsymbol{H}_1=\boldsymbol{u}_1\boldsymbol{v}_1^*$ and $\boldsymbol{H}_1=\boldsymbol{u}_2\boldsymbol{v}_2^*$ with $\boldsymbol{u}_1$, $\boldsymbol{v}_1$, $\boldsymbol{u}_2$, and $\boldsymbol{v}_2$ described in (99) and (100). The proposed phase shift (19) compensates for $\boldsymbol{u}_1$ and $\boldsymbol{v}_2^*$, i.e., $|\boldsymbol{v}_2^*\boldsymbol{\Phi}\boldsymbol{u}_1|=M$, thus it is optimal.

APPENDIX D

Let us introduce an $N_{\mathrm{r}}\times N_{\mathrm{t}}$ matrix $\boldsymbol{A}$ whose (m,n)th entry is

$$[\boldsymbol{A}]_{n,m} = \frac{1}{\sqrt{\mathsf{area}(T_m)\mathsf{area}(R_n)}}\int_{R_n}\int_{T_m}e^{j2\pi(\boldsymbol{t}\cdot\boldsymbol{r})}d\boldsymbol{t}\,d\boldsymbol{r}$$

$$[\boldsymbol{H}_1]_{\ell,m} = \exp\left(-j\frac{2\pi}{\lambda}D_1\right)\exp\left(-j\frac{2\pi}{\lambda}\left(\boldsymbol{e}_{z_1}^\top\begin{bmatrix}x'_\ell\\y'_\ell\\z'_\ell\end{bmatrix}+\frac{1}{2D_1}\left(\left\|\begin{bmatrix}x'_\ell\\y'_\ell\\z'_\ell\end{bmatrix}\right\|^2-\left(\boldsymbol{e}_{z_1}^\top\begin{bmatrix}x'_\ell\\y'_\ell\\z'_\ell\end{bmatrix}\right)^2\right)\right)\right) \tag{97}$$

$$[\boldsymbol{H}_2]_{n,\ell} = \exp\left(-j\frac{2\pi}{\lambda}D_2\right)\exp\left(-j\frac{2\pi}{\lambda}\left(-\boldsymbol{e}_{z_2}^\top\begin{bmatrix}x'_\ell\\y'_\ell\\z'_\ell\end{bmatrix}+\frac{1}{2D_2}\left(\left\|\begin{bmatrix}x'_\ell\\y'_\ell\\z'_\ell\end{bmatrix}\right\|^2-\left(\boldsymbol{e}_{z_1}^\top\begin{bmatrix}x'_\ell\\y'_\ell\\z'_\ell\end{bmatrix}\right)^2\right)\right)\right) \tag{98}$$

$$[\boldsymbol{u}_1]_\ell = \exp\left(-j\frac{2\pi}{\lambda}\left(\boldsymbol{e}_{z_1}^\top\begin{bmatrix}x'_\ell\\y'_\ell\\z'_\ell\end{bmatrix}+\frac{1}{2D_1}\left(\left\|\begin{bmatrix}x'_\ell\\y'_\ell\\z'_\ell\end{bmatrix}\right\|^2-\left(\boldsymbol{e}_{z_1}^\top\begin{bmatrix}x'_\ell\\y'_\ell\\z'_\ell\end{bmatrix}\right)^2\right)\right)\right) \qquad [\boldsymbol{v}_1^*]_m = \exp\left(-j\frac{2\pi}{\lambda}D_1\right) \tag{99}$$

$$[\boldsymbol{u}_2]_n = \exp\left(-j\frac{2\pi}{\lambda}D_2\right) \qquad [\boldsymbol{v}_2^*]_\ell = \exp\left(-j\frac{2\pi}{\lambda}\left(-\boldsymbol{e}_{z_2}^\top\begin{bmatrix}x'_\ell\\y'_\ell\\z'_\ell\end{bmatrix}+\frac{1}{2D_2}\left(\left\|\begin{bmatrix}x'_\ell\\y'_\ell\\z'_\ell\end{bmatrix}\right\|^2-\left(\boldsymbol{e}_{z_1}^\top\begin{bmatrix}x'_\ell\\y'_\ell\\z'_\ell\end{bmatrix}\right)^2\right)\right)\right) \tag{100}$$

$$\left[\boldsymbol{A}-\sqrt{\frac{\mathsf{area}(T)\mathsf{area}(R)}{N_\mathrm{t}N_\mathrm{r}}}\boldsymbol{H}\right]_{n,m} = \sqrt{\frac{N_\mathrm{t}N_\mathrm{r}}{\mathsf{area}(T)\mathsf{area}(R)}}\underbrace{\left(\int_{R_n}\int_{T_m}e^{j2\pi(\boldsymbol{t}\cdot\boldsymbol{r})}d\boldsymbol{t}\,d\boldsymbol{r}-\frac{\mathsf{area}(T)\mathsf{area}(R)}{N_\mathrm{t}N_\mathrm{r}}e^{j2\pi(\boldsymbol{t}_m\cdot\boldsymbol{r}_n)}\right)}_{\text{error of midpoint rule}} \tag{104}$$

$$= \sqrt{\frac{N_\mathrm{t}N_\mathrm{r}}{\mathsf{area}(T)\mathsf{area}(R)}}\int_{R_n}\int_{T_m}e^{j2\pi(\boldsymbol{t}\cdot\boldsymbol{r})}d\boldsymbol{t}\,d\boldsymbol{r} \tag{101}$$

where T_m and R_n are transmit and receive grids cells containing $\boldsymbol{t}_m$ and $\boldsymbol{r}_n$, respectively. Such $\boldsymbol{A}$ is a representation of $\mathcal{H}$ in the sense that

$$\|\boldsymbol{\sigma}(\mathcal{H})-\boldsymbol{\sigma}(\boldsymbol{A})\| \le \sqrt{\|\mathcal{H}\|_\mathrm{HS}^2-\|\boldsymbol{A}\|_\mathrm{F}^2} \tag{102}$$

and

$$\left\|\boldsymbol{\sigma}(\boldsymbol{A})-\sqrt{\frac{\mathsf{area}(T)\mathsf{area}(R)}{N_\mathrm{t}N_\mathrm{r}}}\boldsymbol{\sigma}(\boldsymbol{H})\right\| \le \left\|\boldsymbol{A}-\sqrt{\frac{\mathsf{area}(T)\mathsf{area}(R)}{N_\mathrm{t}N_\mathrm{r}}}\boldsymbol{H}\right\|_\mathrm{F} \tag{103}$$

from [66, Thm 3] and [67, Thm 5], respectively. Invoking the triangle inequality,

$$\left\|\boldsymbol{\sigma}(\mathcal{H})-\sqrt{\frac{\mathsf{area}(T)\mathsf{area}(R)}{N_\mathrm{t}N_\mathrm{r}}}\boldsymbol{\sigma}(\boldsymbol{H})\right\| \le \sqrt{\|\mathcal{H}\|_\mathrm{HS}^2-\|\boldsymbol{A}\|_\mathrm{F}^2}+\left\|\boldsymbol{A}-\sqrt{\frac{\mathsf{area}(T)\mathsf{area}(R)}{N_\mathrm{t}N_\mathrm{r}}}\boldsymbol{H}\right\|_\mathrm{F}.$$

We first evaluate the second term in (104), which relates to the error in a midpoint rule for four-dimensional integration. Increasing $N_{\mathrm{t},x}, N_{\mathrm{t},y}, N_{\mathrm{r},x}, N_{\mathrm{r},y}$ proportionally to N, (104) is $\mathcal{O}(N^{-4})$. Thus, the second term is $\mathcal{O}(N^{-2})$. Applying the triangle inequality again, $\|\boldsymbol{A}\|_\mathrm{F}$ is equal to or larger than

$$\left\|\sqrt{\frac{\mathsf{area}(T)\mathsf{area}(R)}{N_\mathrm{t}N_\mathrm{r}}}\boldsymbol{H}\right\|_\mathrm{F}-\left\|\boldsymbol{A}-\sqrt{\frac{\mathsf{area}(T)\mathsf{area}(R)}{N_\mathrm{t}N_\mathrm{r}}}\boldsymbol{H}\right\|_\mathrm{F},$$

hence $\|\boldsymbol{A}\|_\mathrm{F} = \sqrt{\mathsf{area}(T)\mathsf{area}(R)}-\mathcal{O}(N^{-2})$. This means that the first term is

$$\sqrt{\mathsf{area}(T)\mathsf{area}(R)-(\sqrt{\mathsf{area}(T)\mathsf{area}(R)}-\mathcal{O}(N^{-2}))^2},$$

which is clearly $\mathcal{O}(N^{-1})$, and (61) therefore follows.

Appendix E

The identity in (73) can be derived as

$$r^{-2}\sum_n\lambda_n(\mathcal{H}_\mathsf{eff}\mathcal{H}_\mathsf{eff}^*) \tag{105}$$

$$= r^{-2}\sum_n\sigma_n^2(\mathcal{H}_\mathsf{eff}) \tag{106}$$

$$= r^{-2}\int_R\int_T\left|\int_{rI}e^{j2\pi((\boldsymbol{t}+\boldsymbol{r})\cdot\boldsymbol{i})}d\boldsymbol{i}\right|^2d\boldsymbol{t}d\boldsymbol{r} \tag{107}$$

$$= r^{-2}\int_R\int_T\int_{rI}\int_{rI}e^{j2\pi((\boldsymbol{t}+\boldsymbol{r})\cdot(\boldsymbol{i}-\boldsymbol{i}'))}d\boldsymbol{i}d\boldsymbol{i}'d\boldsymbol{t}d\boldsymbol{r} \tag{108}$$

$$= \int_R\int_T\int_I\int_{r(\boldsymbol{s}-I)}e^{j2\pi((\boldsymbol{t}+\boldsymbol{r})\cdot\boldsymbol{s}')}d\boldsymbol{s}'d\boldsymbol{s}d\boldsymbol{t}d\boldsymbol{r} \tag{109}$$

$$\to \mathsf{area}(I)\int\left(\int_T e^{j2\pi(\boldsymbol{t}\cdot\boldsymbol{s}')}d\boldsymbol{t}\right)\left(\int_R e^{j2\pi(\boldsymbol{r}\cdot\boldsymbol{s}')}d\boldsymbol{r}\right)d\boldsymbol{s}' \tag{110}$$

$$= \mathsf{area}(I)\int(\mathcal{F}^{-1}\mathbf{1}_T)(\boldsymbol{s}')(\mathcal{F}^{-1}\mathbf{1}_R)(\boldsymbol{s}')d\boldsymbol{s}' \tag{111}$$

$$= \mathsf{area}(I)(\mathbf{1}_T*\mathbf{1}_R)(\mathbf{0}) \tag{112}$$

$$= \mathsf{area}(I)\mathsf{area}(T\cap(-R)), \tag{113}$$

where the change of variable $\boldsymbol{i} = r\boldsymbol{s}, \boldsymbol{i}' = r\boldsymbol{s}-\boldsymbol{s}'$ is used in (109) and the convolution theorem is applied in (112).

The identity in (74), in turn, can be derived as (114)–(124), with the variable changes $\boldsymbol{i} = r\boldsymbol{s}, \boldsymbol{i}' = r\boldsymbol{s}-\boldsymbol{s}', \boldsymbol{i}'' = r\boldsymbol{s}-\boldsymbol{s}'', \boldsymbol{i}''' = r\boldsymbol{s}-\boldsymbol{s}'''$ applied in (119).

Appendix F

See (125)–(128).

$$
\begin{aligned}
& r^{-2}\sum_n \lambda_n^2(\mathcal{H}_{\mathsf{eff}}\mathcal{H}_{\mathsf{eff}}^*) && (114)\\
&= r^{-2}\sum_n \sigma_n^2(\mathcal{H}_{\mathsf{eff}}\mathcal{H}_{\mathsf{eff}}^*) && (115)\\
&= r^{-2}\int_R\int_R\left|\int_T\left(\int_{rI}\exp(j2\pi((\boldsymbol{t}+\boldsymbol{r})\cdot\boldsymbol{i}))d\boldsymbol{i}\right)\left(\int_{rI}\exp(-j2\pi((\boldsymbol{t}+\boldsymbol{r}')\cdot\boldsymbol{i}'))d\boldsymbol{i}'\right)d\boldsymbol{t}\right|^2 d\boldsymbol{r}d\boldsymbol{r}' && (116)\\
&= r^{-2}\int_R\int_R\int_T\int_T\left(\int_{rI}\exp(j2\pi((\boldsymbol{t}+\boldsymbol{r})\cdot\boldsymbol{i}))d\boldsymbol{i}\right)\left(\int_{rI}\exp(-j2\pi((\boldsymbol{t}+\boldsymbol{r}')\cdot\boldsymbol{i}'))d\boldsymbol{i}'\right)\\
&\quad\cdot\left(\int_{rI}\exp(-j2\pi((\boldsymbol{t}'+\boldsymbol{r})\cdot\boldsymbol{i}''))d\boldsymbol{i}''\right)\left(\int_{rI}\exp(j2\pi((\boldsymbol{t}'+\boldsymbol{r}')\cdot\boldsymbol{i}'''))d\boldsymbol{i}'''\right)d\boldsymbol{t}d\boldsymbol{t}'d\boldsymbol{r}d\boldsymbol{r}' && (117)\\
&= r^{-2}\int_R\int_R\int_T\int_T\int_{rI}\int_{rI}\int_{rI}\int_{rI}\exp\big(j2\pi(\boldsymbol{t}\cdot(\boldsymbol{i}-\boldsymbol{i}')+\boldsymbol{r}\cdot(\boldsymbol{i}-\boldsymbol{i}'')+\boldsymbol{t}'\cdot(-\boldsymbol{i}''+\boldsymbol{i}''')\\
&\quad+\boldsymbol{r}'\cdot(-\boldsymbol{i}'+\boldsymbol{i}'''))\big)d\boldsymbol{i}d\boldsymbol{i}'d\boldsymbol{i}''d\boldsymbol{i}'''d\boldsymbol{t}d\boldsymbol{t}'d\boldsymbol{r}d\boldsymbol{r}' && (118)\\
&= \int_R\int_R\int_T\int_T\int_I\int_{r(\boldsymbol{s}-I)}\int_{r(\boldsymbol{s}-I)}\int_{r(\boldsymbol{s}-I)}\exp\big(j2\pi(\boldsymbol{t}\cdot\boldsymbol{s}'+\boldsymbol{r}\cdot\boldsymbol{s}''+\boldsymbol{t}'\cdot(\boldsymbol{s}''-\boldsymbol{s}''')\\
&\quad+\boldsymbol{r}'\cdot(\boldsymbol{s}'-\boldsymbol{s}'''))\big)d\boldsymbol{s}'''d\boldsymbol{s}''d\boldsymbol{s}'d\boldsymbol{s}d\boldsymbol{t}d\boldsymbol{t}'d\boldsymbol{r}d\boldsymbol{r}' && (119)\\
&\to \mathsf{area}(I)\int_R\int_R\int_T\int_T\left(\int\exp(j2\pi(\boldsymbol{t}+\boldsymbol{r}')\cdot\boldsymbol{s}')d\boldsymbol{s}'\right)\left(\int\exp(j2\pi(\boldsymbol{t}'+\boldsymbol{r})\cdot\boldsymbol{s}'')d\boldsymbol{s}''\right)\\
&\quad\cdot\left(\int\exp(-j2\pi(\boldsymbol{t}'+\boldsymbol{r}')\cdot\boldsymbol{s}''')d\boldsymbol{s}'''\right)d\boldsymbol{t}d\boldsymbol{t}'d\boldsymbol{r}d\boldsymbol{r}' && (120)\\
&= \mathsf{area}(I)\int_R\int_R\int_T\int_T\delta(\boldsymbol{t}+\boldsymbol{r}')\delta(\boldsymbol{t}'+\boldsymbol{r})\delta(\boldsymbol{t}'+\boldsymbol{r}')d\boldsymbol{t}d\boldsymbol{t}'d\boldsymbol{r}d\boldsymbol{r}' && (121)\\
&= \mathsf{area}(I)\int_R\int_T\underbrace{\left(\int_T\delta(\boldsymbol{t}+\boldsymbol{r}')d\boldsymbol{t}\right)}_{\mathbf{1}_{-T}(\boldsymbol{r}')}\underbrace{\left(\int_R\delta(\boldsymbol{t}'+\boldsymbol{r})d\boldsymbol{r}\right)}_{\mathbf{1}_{-R}(\boldsymbol{t}')}\delta(\boldsymbol{t}'+\boldsymbol{r}')d\boldsymbol{t}'d\boldsymbol{r}' && (122)\\
&= \mathsf{area}(I)\int_{R\cap -T}\underbrace{\int_{T\cap -R}\delta(\boldsymbol{t}'+\boldsymbol{r}')d\boldsymbol{t}'}_{\mathbf{1}_{R\cap -T}(\boldsymbol{r}')}d\boldsymbol{r}' && (123)\\
&= \mathsf{area}(I)\mathsf{area}(T\cap -R) && (124)
\end{aligned}
$$

$$
\begin{aligned}
\mathsf{DOF}^{\mathsf{up}} &= \mathsf{area}(I)\min\big(\mathsf{area}(T),\mathsf{area}(R)\big) && (125)\\
&= \mathsf{area}\left(\frac{1}{\sqrt{\lambda D_1}}\left(L_{\mathrm{i},x}\left[-\frac{1}{2},\frac{1}{2}\right]\times L_{\mathrm{i},y}\left[-\frac{1}{2},\frac{1}{2}\right]\right)\right)\\
&\quad\cdot\min\left(\mathsf{area}\left(\frac{1}{\sqrt{\lambda D_1}}\begin{bmatrix}\boldsymbol{e}_{\tilde{x}'}^\top\\ \boldsymbol{e}_{\tilde{y}'}^\top\end{bmatrix}(\boldsymbol{I}-\boldsymbol{e}_{z_1}\boldsymbol{e}_{z_1}^\top)\begin{bmatrix}\boldsymbol{e}_{\tilde{x}} & \boldsymbol{e}_{\tilde{y}}\end{bmatrix}\left(L_{\mathrm{t},x}\left[-\frac{1}{2},\frac{1}{2}\right]\times L_{\mathrm{t},y}\left[-\frac{1}{2},\frac{1}{2}\right]\right)\right),\right.\\
&\qquad\left.\mathsf{area}\left(\frac{D_1}{D_2}\cdot\frac{1}{\sqrt{\lambda D_1}}\begin{bmatrix}\boldsymbol{e}_{\tilde{x}'}^\top\\ \boldsymbol{e}_{\tilde{y}'}^\top\end{bmatrix}(\boldsymbol{I}-\boldsymbol{e}_{z_2}\boldsymbol{e}_{z_2}^\top)\begin{bmatrix}\boldsymbol{e}_{\tilde{x}''} & \boldsymbol{e}_{\tilde{y}''}\end{bmatrix}\left(L_{\mathrm{r},x}\left[-\frac{1}{2},\frac{1}{2}\right]\times L_{\mathrm{r},y}\left[-\frac{1}{2},\frac{1}{2}\right]\right)\right)\right) && (126)\\
&= \frac{L_{\mathrm{i},x}L_{\mathrm{i},y}}{\lambda D_1}\min\left(\frac{L_{\mathrm{t},x}L_{\mathrm{t},y}}{\lambda D_1}\left|\det\left(\begin{bmatrix}\boldsymbol{e}_{\tilde{x}'}^\top\\ \boldsymbol{e}_{\tilde{y}'}^\top\end{bmatrix}\begin{bmatrix}\boldsymbol{e}_{x_1} & \boldsymbol{e}_{y_1}\end{bmatrix}\right)\right|\left|\det\left(\begin{bmatrix}\boldsymbol{e}_{\tilde{x}}^\top\\ \boldsymbol{e}_{\tilde{y}}^\top\end{bmatrix}\begin{bmatrix}\boldsymbol{e}_{x_1} & \boldsymbol{e}_{y_1}\end{bmatrix}\right)\right|,\right.\\
&\qquad\left.\frac{L_{\mathrm{r},x}L_{\mathrm{r},y}D_1}{\lambda D_2^2}\left|\det\left(\begin{bmatrix}\boldsymbol{e}_{\tilde{x}'}^\top\\ \boldsymbol{e}_{\tilde{y}'}^\top\end{bmatrix}\begin{bmatrix}\boldsymbol{e}_{x_2} & \boldsymbol{e}_{y_2}\end{bmatrix}\right)\right|\left|\det\left(\begin{bmatrix}\boldsymbol{e}_{\tilde{x}''}^\top\\ \boldsymbol{e}_{\tilde{y}''}^\top\end{bmatrix}\begin{bmatrix}\boldsymbol{e}_{x_2} & \boldsymbol{e}_{y_2}\end{bmatrix}\right)\right|\right) && (127)\\
&= \min\Bigg(\underbrace{\frac{L_{\mathrm{i},x}L_{\mathrm{i},y}}{\lambda D_1}\left|\det\left(\begin{bmatrix}\boldsymbol{e}_{\tilde{x}'}^\top\\ \boldsymbol{e}_{\tilde{y}'}^\top\end{bmatrix}\begin{bmatrix}\boldsymbol{e}_{x_1} & \boldsymbol{e}_{y_1}\end{bmatrix}\right)\right|}_{\frac{A_{\mathrm{i}}}{\lambda D_1}}\cdot\underbrace{\frac{L_{\mathrm{t},x}L_{\mathrm{t},y}}{\lambda D_1}\left|\det\left(\begin{bmatrix}\boldsymbol{e}_{\tilde{x}}^\top\\ \boldsymbol{e}_{\tilde{y}}^\top\end{bmatrix}\begin{bmatrix}\boldsymbol{e}_{x_1} & \boldsymbol{e}_{y_1}\end{bmatrix}\right)\right|}_{\frac{A_{\mathrm{t}}}{\lambda D_1}},\\
&\qquad\underbrace{\frac{L_{\mathrm{i},x}L_{\mathrm{i},y}}{\lambda D_2}\left|\det\left(\begin{bmatrix}\boldsymbol{e}_{\tilde{x}'}^\top\\ \boldsymbol{e}_{\tilde{y}'}^\top\end{bmatrix}\begin{bmatrix}\boldsymbol{e}_{x_2} & \boldsymbol{e}_{y_2}\end{bmatrix}\right)\right|}_{\frac{A_{\mathrm{i}}'}{\lambda D_2}}\cdot\underbrace{\frac{L_{\mathrm{r},x}L_{\mathrm{r},y}}{\lambda D_2}\left|\det\left(\begin{bmatrix}\boldsymbol{e}_{\tilde{x}''}^\top\\ \boldsymbol{e}_{\tilde{y}''}^\top\end{bmatrix}\begin{bmatrix}\boldsymbol{e}_{x_2} & \boldsymbol{e}_{y_2}\end{bmatrix}\right)\right|}_{\frac{A_{\mathrm{r}}}{\lambda D_2}}\Bigg). && (128)
\end{aligned}
$$

REFERENCES

[1] H.-J. Song and T. Nagatsuma, "Present and future of terahertz communications," *IEEE Trans. Terahertz Sci. Technol.*, vol. 1, no. 1, pp. 256–263, 2011.

[2] T. S. Rappaport, Y. Xing, O. Kanhere, S. Ju, A. Madanayake, S. Mandal, A. Alkhateeb, and G. C. Trichopoulos, "Wireless communications and applications above 100 GHz: Opportunities and challenges for 6G and beyond," *IEEE Access*, vol. 7, pp. 78 729–78 757, 2019.

[3] V. Petrov, T. Kurner, and I. Hosako, "IEEE 802.15. 3d: First standardization efforts for sub-terahertz band communications toward 6G," *IEEE Commun. Mag.*, vol. 58, no. 11, pp. 28–33, 2020.

[4] I. Dan, P. Szriftgiser, E. Peytavit, J.-F. Lampin, M. Zegaoui, M. Zaknoune, G. Ducournau, and I. Kallfass, "A 300-GHz wireless link employing a photonic transmitter and an active electronic receiver with a transmission bandwidth of 54 GHz," *IEEE Trans. Terahertz Sci. Technol.*, vol. 10, no. 3, pp. 271–281, 2020.

[5] P. F. Driessen and G. Foschini, "On the capacity formula for multiple input-multiple output wireless channels: A geometric interpretation," *IEEE Trans. Commun.*, vol. 47, no. 2, pp. 173–176, Feb. 1999.

[6] F. Bøhagen, P. Orten, and G. Øien, "Construction and capacity analysis of high-rank line-of-sight MIMO channels," in *Proc. IEEE Wireless Commun. Netw. Conf.*, Mar. 2005, pp. 432–437.

[7] P. Larsson, "Lattice array receiver and sender for spatially orthonormal MIMO communication," in *Proc. IEEE Veh. Technol. Conf.*, May 2005, pp. 192–196.

[8] I. Sarris and A. R. Nix, "Design and performance assessment of high-capacity MIMO architectures in the presence of a line-of-sight component," *IEEE Trans. Veh. Technol.*, vol. 56, no. 4, pp. 2194–2202, Jul. 2007.

[9] C. Sheldon, E. Torkildson, M. Seo, U. Madhow, and M. Rodwell, "Four-channel spatial multiplexing over a millimeter-wave line-of-sight link," in *IEEE MTT-S Int'l Microw. Symp. Dig.*, Jun. 2009, pp. 389–392.

[10] L. Bao and B.-E. Olsson, "Methods and measurements of channel phase difference in 2x2 microwave LOS-MIMO systems," in *Proc. IEEE Int'l Conf. Commun.*, Jun. 2015, pp. 1358–1363.

[11] T. Hälsig, D. Cvetkovski, E. Grass, and B. Lankl, "Measurement results for millimeter wave pure LOS MIMO channels," in *Proc. IEEE Wireless Commun. Netw. Conf.* IEEE, 2017, pp. 1–6.

[12] Y. Yan, P. Bondalapati, A. Tiwari, C. Xia, A. Cashion, D. Zhang, Q. Tang, and M. Reed, "11-Gbps broadband modem-agnostic line-of-sight MIMO over the range of 13 km," in *IEEE Global Commun. Conf.*, 2018, pp. 1–7.

[13] G. Sellin, M. Edberg, M. Berggren, M. Coldrey, J. Edstam, D. Eriksson, J. Flodin, J. Hansryd, A. Olsson, M. Ohberg, and D. Siomos, "Ericsson microwave outlook," Ericsson, Tech. Rep., 2019.

[14] D. Cvetkovski, T. Hälsig, B. Lankl, and E. Grass, "Four-stream line-of-sight spatial multiplexing for 60 GHz backhaul applications," *IEEE Wireless Commun. Lett.*, 2021.

[15] J.-S. Jiang and M. A. Ingram, "Spherical-wave model for short-range MIMO," *IEEE Trans. Commun.*, vol. 53, no. 9, pp. 1534–1541, 2005.

[16] F. Bohagen, P. Orten, and G. E. Oien, "On spherical vs. plane wave modeling of line-of-sight MIMO channels," *IEEE Tran. Commun.*, vol. 57, no. 3, pp. 841–849, 2009.

[17] E. Torkildson, U. Madhow, and M. Rodwell, "Indoor millimeter wave MIMO: Feasibility and performance," *IEEE Trans. Wireless Commun.*, vol. 10, no. 12, pp. 4150–4160, 2011.

[18] H. Do, N. Lee, and A. Lozano, "Reconfigurable ULAs for line-of-sight MIMO transmission," *IEEE Trans. Wireless Commun.*, vol. 20, no. 5, pp. 2933–2947, 2020.

[19] ——, "Capacity of line-of-sight MIMO channels," in *Int'l Symp. Inform. Theory (ISIT'20)*, 2020, pp. 2044–2048.

[20] H. Do, S. Cho, J. Park, H.-J. Song, N. Lee, and A. Lozano, "Terahertz line-of-sight MIMO communication: Theory and practical challenges," *IEEE Commun. Mag.*, vol. 59, no. 3, pp. 104–109, 2021.

[21] H. Do, N. Lee, and A. Lozano, "Rotatable URAs for line-of-sight MIMO transmission," in *IEEE Global Commun. Conf. (GLOBECOM)*, 2021.

[22] R. W. Heath, Jr. and A. Lozano, *Foundations of MIMO Communication*. Cambridge University Press, 2018.

[23] D. A. Miller, "Communicating with waves between volumes: evaluating orthogonal spatial channels and limits on coupling strengths," *Applied Optics*, vol. 39, no. 11, pp. 1681–1699, 2000.

[24] A. Pizzo and A. Lozano, "On Landau's eigenvalue theorem for line-of-sight MIMO channels," *IEEE Wireless Commun. Lett.*, 2023.

[25] A. Poon, R. W. Brodersen, and D. N. C. Tse, "Degrees of freedom in multiple-antenna channels: A signal space approach," *IEEE Trans. Inform. Theory*, vol. 51, no. 2, pp. 523–536, 2005.

[26] M. Desgroseilliers, O. Lévêque, and E. Preissmann, "Spatial degrees of freedom of MIMO systems in line-of-sight environment," in *IEEE Int'l Symp. Inform. Theory (ISIT)*, 2013, pp. 834–838.

[27] C. Liaskos, S. Nie, A. Tsioliaridou, A. Pitsillides, S. Ioannidis, and I. Akyildiz, "A new wireless communication paradigm through software-controlled metasurfaces," *IEEE Commun. Mag.*, vol. 56, no. 9, pp. 162–169, 2018.

[28] Q. Wu and R. Zhang, "Towards smart and reconfigurable environment: Intelligent reflecting surface aided wireless network," *IEEE Commun. Mag.*, vol. 58, no. 1, pp. 106–112, 2019.

[29] E. Basar, M. Di Renzo, J. De Rosny, M. Debbah, M.-S. Alouini, and R. Zhang, "Wireless communications through reconfigurable intelligent surfaces," *IEEE Access*, vol. 7, pp. 116 753–116 773, 2019.

[30] X. Yu, D. Xu, and R. Schober, "MISO wireless communication systems via intelligent reflecting surfaces," in *IEEE/CIC Int'l Conf. Commun. China*, 2019, pp. 735–740.

[31] S. Zhang and R. Zhang, "Capacity characterization for intelligent reflecting surface aided MIMO communication," *IEEE J. Sel. Areas Commun.*, vol. 38, no. 8, pp. 1823–1838, 2020.

[32] S. Gong, X. Lu, D. T. Hoang, D. Niyato, L. Shu, D. I. Kim, and Y.-C. Liang, "Toward smart wireless communications via intelligent reflecting surfaces: A contemporary survey," *IEEE Commun. Surv. & Tut.*, vol. 22, no. 4, pp. 2283–2314, 2020.

[33] M. Najafi, V. Jamali, R. Schober, and H. V. Poor, "Physics-based modeling and scalable optimization of large intelligent reflecting surfaces," *IEEE Trans. Commun.*, vol. 69, no. 4, pp. 2673–2691, 2020.

[34] N. S. Perović, L.-N. Tran, M. Di Renzo, and M. F. Flanagan, "Achievable rate optimization for MIMO systems with reconfigurable intelligent surfaces," *IEEE Trans. Wireless Commun.*, 2021.

[35] C. Cai, X. Yuan, W. Yan, Z. Huang, Y.-C. Liang, and W. Zhang, "Hierarchical passive beamforming for reconfigurable intelligent surface aided communications," *IEEE Wireless Commun. Lett.*, vol. 10, no. 9, pp. 1909–1913, 2021.

[36] K. Dovelos, S. D. Assimonis, H. Quoc Ngo, B. Bellalta, and M. Matthaiou, "Intelligent reflecting surfaces at terahertz bands: Channel modeling and analysis," in *IEEE Int'l Conf. Commun. Workshops*, 2021, pp. 1–6.

[37] J. Choi, G. Kwon, and H. Park, "Multiple intelligent reflecting surfaces for capacity maximization in LOS MIMO systems," *IEEE Wireless Commun. Lett.*, 2021.

[38] M. Zhang and X. Yuan, "Intelligent reflecting surface aided MIMO with cascaded line-of-sight links: Channel modelling and capacity analysis," *arXiv preprint arXiv:2109.08913*, 2021.

[39] W. Khawaja, O. Ozdemir, Y. Yapici, I. Guvenc, and Y. Kakishima, "Coverage enhancement for mmWave communications using passive reflectors," in *Global Symp. Millimeter Waves*, 2018, pp. 1–6.

[40] J. W. Goodman, *Introduction to Fourier Optics*. McGraw-Hill, 1968.

[41] W. Southwell, "Validity of the Fresnel approximation in the near field," *Journal of the Optical Society of America*, vol. 71, no. 1, pp. 7–14, 1981.

[42] S. Mezouari and A. R. Harvey, "Validity of Fresnel and Fraunhofer approximations in scalar diffraction," *Journal of Optics A: Pure and Applied Optics*, vol. 5, no. 4, p. S86, 2003.

[43] E. Telatar, "Capacity of multi-antenna Gaussian channels," *European Trans. Telecommun.*, vol. 10, no. 6, pp. 585–595, 1999.

[44] A. Tulino, A. Lozano, and S. Verdú, "MIMO capacity with channel state information at the transmitter," in *IEEE Int'l Symp. Spread Spectrum Techn. and Applic. (ISSSTA'04)*, 2004.

[45] Z. Fang, Y. Hua, and J. C. Koshy, "Joint source and relay optimization for a non-regenerative MIMO relay," in *IEEE Workshop Sensor Array Multichannel Process.*, 2006, pp. 239–243.

[46] Ö. Özdogan, E. Björnson, and E. G. Larsson, "Intelligent reflecting surfaces: Physics, propagation, and pathloss modeling," *IEEE Wireless Commun. Lett.*, vol. 9, no. 5, pp. 581–585, 2019.

[47] M. Di Renzo, F. Danufane, X. Xi, J. De Rosny, and S. Tretyakov, "Analytical modeling of the path-loss for reconfigurable intelligent surfaces–anomalous mirror or scatterer?" in *IEEE Int'l Workshop Signal Process. Adv. Wireless Commun.*, 2020, pp. 1–5.

[48] A. Pizzo, T. L. Marzetta, and L. Sanguinetti, "Spatially-stationary model for holographic MIMO small-scale fading," *IEEE J. Sel. Areas Commun.*, vol. 38, no. 9, pp. 1964–1979, 2020.

[49] C. Huang, S. Hu, G. C. Alexandropoulos, A. Zappone, C. Yuen, R. Zhang, M. Di Renzo, and M. Debbah, "Holographic MIMO surfaces

for 6G wireless networks: Opportunities, challenges, and trends," *IEEE Wireless Commun.*, vol. 27, no. 5, pp. 118–125, 2020.
[50] C. Heil, *Metrics, Norms, Inner Products, and Operator Theory*. Springer, 2018.
[51] H. Landau, "On Szegö's eigenvalue distribution theorem and non-Hermitian kernels," *Journal d'Analyse Mathématique*, vol. 28, no. 1, pp. 335–357, 1975.
[52] E. Biglieri, G. Taricco, and A. Tulino, "How far away is infinity? using asymptotic analyses in multiple-antenna systems," in *IEEE Int'l Symp. Spread Spectr. Techn. Appl.*, vol. 1. IEEE, 2002, pp. 1–6.
[53] S. Abeywickrama, R. Zhang, Q. Wu, and C. Yuen, "Intelligent reflecting surface: Practical phase shift model and beamforming optimization," *IEEE Trans. Commun.*, vol. 68, no. 9, pp. 5849–5863, 2020.
[54] W. Tang, M. Z. Chen, X. Chen, J. Y. Dai, Y. Han, M. Di Renzo, Y. Zeng, S. Jin, Q. Cheng, and T. J. Cui, "Wireless communications with reconfigurable intelligent surface: Path loss modeling and experimental measurement," *IEEE Trans. Wireless Commun.*, 2020.
[55] S. E. Hosseininejad, K. Rouhi, M. Neshat, A. Cabellos-Aparicio, S. Abadal, and E. Alarcón, "Digital metasurface based on graphene: An application to beam steering in terahertz plasmonic antennas," *IEEE Trans. Nanotechnol.*, vol. 18, pp. 734–746, 2019.
[56] K. Rouhi, H. Rajabalipanah, and A. Abdolali, "Multi-bit graphene-based bias-encoded metasurfaces for real-time terahertz wavefront shaping: From controllable orbital angular momentum generation toward arbitrary beam tailoring," *Carbon*, vol. 149, pp. 125–138, 2019.
[57] H. Do, N. Lee, and A. Lozano, "DOF augmentation via IRS for line-of-sight communication," in *Asilomar Conf. on Signals, Systems and Computers*, 2022.
[58] S. Hu, F. Rusek, and O. Edfors, "Beyond massive MIMO: The potential of data transmission with large intelligent surfaces," *IEEE Trans. Signal Process.*, vol. 66, no. 10, pp. 2746–2758, 2018.
[59] D. Dardari, "Communicating with large intelligent surfaces: Fundamental limits and models," *IEEE J. Sel. Areas Commun.*, vol. 38, no. 11, pp. 2526–2537, 2020.
[60] E. Björnson and L. Sanguinetti, "Power scaling laws and near-field behaviors of massive MIMO and intelligent reflecting surfaces," *IEEE Open J. Commun. Soc.*, vol. 1, pp. 1306–1324, 2020.

Heedong Do (S'20) received a B.S. in mathematics and a M.S. in electrical engineering from Pohang University of Science & Technology (POSTECH), Pohang, Korea, in 2018 and 2020, respectively. He is currently a Ph.D. candidate.

[61] Q. Sun, D. C. Cox, A. Lozano, and H. C. Huang, "Training-based channel estimation for continuous flat fading BLAST," in *IEEE Int'l Conf. Commun. (ICC)*, 2002.
[62] A. W. Marshall, I. Olkin, and B. C. Arnold, *Inequalities: theory of majorization and its applications*. Springer, 1979, vol. 143.
[63] T. Ando, "Majorizations and inequalities in matrix theory," *Linear Algebra and its Applications*, vol. 199, pp. 17–67, 1994.
[64] N. Bleistein and R. A. Handelsman, *Asymptotic expansions of integrals*. Ardent Media, 1975.
[65] E. Björnson, Ö. Özdogan, and E. G. Larsson, "Intelligent reflecting surface versus decode-and-forward: How large surfaces are needed to beat relaying?" *IEEE Wireless Commun. Lett.*, vol. 9, no. 2, pp. 244–248, 2019.
[66] P. C. Hansen, "Computation of the singular value expansion," *Computing*, vol. 40, no. 3, pp. 185–199, 1988.
[67] L. Mirsky, "Symmetric gauge functions and unitarily invariant norms," *The Quarterly Journal of Mathematics*, vol. 11, no. 1, pp. 50–59, 1960.

Namyoon Lee (S'11–M'14–SM'20) received a Ph.D. degree from The University of Texas at Austin, in 2014. He was with Communications and Network Research Group, Samsung Advanced Institute of Technology (SAIT), Korea, in 2008-2011 and also with Wireless Communications Research (WCR), Intel Labs, Santa Clara, USA, in 2015-2016. He was with POSTECH, Pohang, Gyeongbuk in 2016-2022, Korea and is currently an Associate Professor at Korea University, Seoul, Korea. He was a recipient of the 2016 IEEE ComSoc Asia–Pacific Outstanding Young Researcher Award. He is currently an Editor for the IEEE Trans. on Wireless Communications and IEEE Trans. on Communications.

Angel Lozano (S'90 – M'99– SM'01 - F'14) received a Ph.D. from Stanford University in 1998. From 1999 to 2008 he was with Bell Labs (Lucent Technologies, now Nokia). He is currently a Professor at Univ. Pompeu Fabra (UPF), Barcelona, and the co-author of the textbook "Foundations of MIMO Communication" (Cambridge University Press, 2019). He serves as Area Editor for the IEEE Trans. on Wireless Communications. He received the 2009 Stephen O. Rice Prize, the 2016 Fred W. Ellersick prize, and the 2016 Communications Society & Information Theory Society joint paper award. He holds an Advanced Grant from the European Research Council and was a 2017 Clarivate Analytics Highly Cited Researcher.